Eidgenössische Technische Hochschule Zürich
Swiss Federal Institute of Technology Zurich

# Towards microwave to optical transduction for superconducting qubits

Master Thesis

Francesco Adinolfi

Laboratory for Solid State Physics
Departement of Physics, D-PHYS
ETH Zürich

**Supervisors:**
Prof. Yiwen Chu
Dr. Hugo Doeleman
Uwe von Lüpke

September 9, 2021

To my family,
to my friends,
to this amazing research group.

# Contents

Chapter 1

# Introduction

Over the last century, the advent of information technologies has deeply reshaped our society, affecting our everyday life, shortening distances and allowing new scientific discoveries. Today, in this interconnected world, quantum science has the potential to change the technology landscape [1]. Quantum cryptography has already revolutionised the landscape of secure information and communication. Quantum sensing gives us the ability to investigate the world around us with a new level of accuracy. Quantum computers will pave the way for future ground-breaking applications from simulating new chemical compounds to exploring the mysterious world of superconductors, from breaking RSA encryption to speeding up search algorithms.

Recent results from Google [2] demonstrated a quantum advantage by performing a difficult task exponentially faster than a classical computer for the first time. Moreover, new progress in the practical implementation of surface codes [3] and recent advances in control of bosonic codes on superconducting devices [4] promise that it will be indeed possible to perform error detection and correction in superconducting circuits, laying the foundation for practical fault tolerant quantum computation.

However, even in a future where fault tolerant superconducting quantum computers are a reality, the question of how can we connect these delicate systems together is still open. Quantum networks could provide new opportunities in the field of quantum simulation, quantum error correction [5] and quantum sensing [6]. Moreover, the creation of a quantum internet could allow to accomplish tasks unfeasible in the classical domain, as the distribution of 'quantum software' [5]. Recently, the direct connection of distant superconducting qubit systems through a five meter microwave coherent link has been demonstrated [7]. Nevertheless, scaling up this technology to long distances and multiple nodes is still a challenge, and it could prove technologically unfeasible.

A solution for connecting multiple spatially separated superconducting quantum systems could be microwave to optical conversion. Unlike microwave electronics, Infrared (IR) fiber communication technology has shown the potential to transmit quantum information with ultra-low loss rates over kilometer distances [8], with negligible added thermal noise at room temperature $T_r$ ($\hbar\omega_{IR} \gg k_b T_r$ with $\omega_{IR}$ the infra red photon frequency). However, conventional electro-optic conversion is highly inefficient [9] and an intermediate system is needed to mediate the transduction process. Mechanical oscillators are a promising candidate, as they host phonon modes that are able to achieve large coupling rates to both microwave [10] and IR photons [11] and can perform conversion with less than a quantum of added noise [12].

A first realization of quantum coherent transduction from a qubit to an IR photon

was recently achieved using a nanomechanical oscillator [13]. This process, nevertheless, yielded a low efficiency due to the limitation on laser power intensity and high mechanical losses. Bulk acoustic oscillators promise to deliver a much higher conversion efficiency due to their much higher quality factors and to their macroscopic dimensions, which allow them to use much higher laser powers. Recent works demonstrated the efficient coupling of two IR modes in an optical cavity through the bulk acoustic phonons of a macroscopic crystal mechanical oscillator [14]. Moreover, recent results in circuit quantum acousto-dynamics [15] outlined the ability to selectively couple superconducting qubits to phonon modes in a bulk acoustic resonator.

The microwave to optical transduction project at Hybrid Quantum Systems Group aims at creating an interface between superconducting circuits and IR photons by exploiting coherent optomechanical and electromechanical interactions. The setup is sketched in Fig. 1.1. The electric field generated by the qubit interacts with the High-Overtone Bulk Acoustic Resonator (HBAR) device, inducing stress in its piezoelectric film and creating bulk acoustic waves into the crystal. The phonon generated in this process can then interact with the IR photons inside the optical cavity through Brillouin scattering. This leads to the creation of a higher frequency IR photon, completing the conversion process.

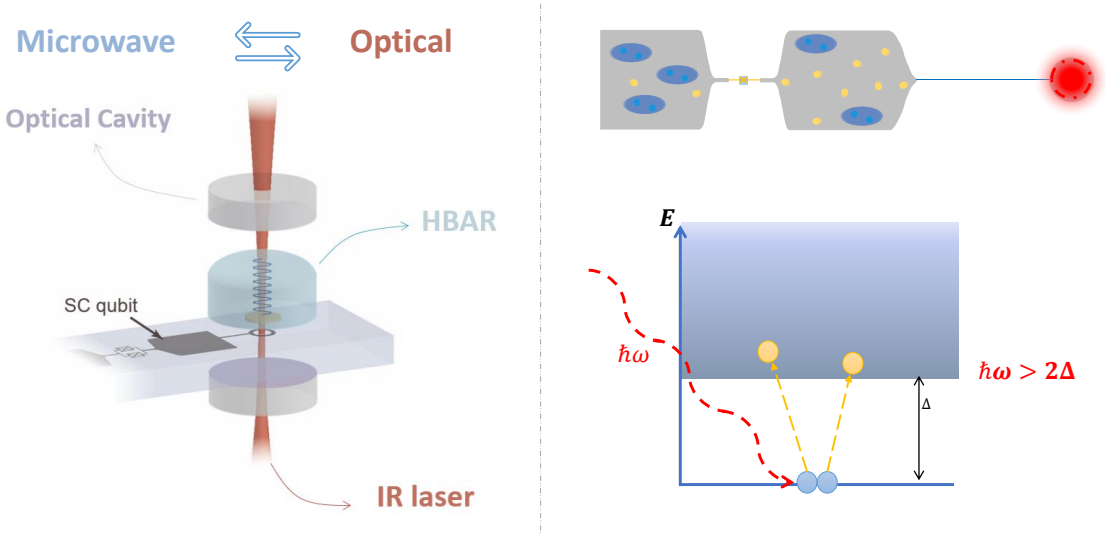


Figure 1.1.: **Left** Sketch of the microwave to optical transduction process. The transmon qubit electric field induces stress into the piezoelectric film (gray) of the HBAR. This generates a phonons into the crystal (in light blue) that interacts with the IR light (in red) confined inside the optical cavity. **Right** Qubit under IR light illumination, with a sketch of band structure of a superconductor. IR photons (red line) are absorbed by Cooper pairs (in blue) and generate quasiparticles (in yellow) and phonons (not shown).

This Master thesis tackles two different challenges related to this conversion scheme.

From the setup of Fig. 1.1 it is clear that one of the challenges of the transduction process lies in IR light shining near the qubit device.
IR photons can be absorbed by Cooper pairs, breaking them and generating quasiparticles in the superconductor. This can lead to many detrimental effects, as unwanted excitations or the increase of the decay and decoherence qubit rates $\Gamma_1$, $\Gamma_2$ [16]. The first part of this report is devoted to the study of this phenomenon by first investigating the effect of IR light on a simple electrical resonator and then on a superconducting transmon qubit.

The second direction pursued aims to design a circuit QED platform compatible with an IR optical cavity. To ensure the success of the transduction experiment it is important to manufacture qubit with a frequency matching the HBAR Brillouin frequency. It is also necessary to design a qubit control and readout platform respecting the tight space requirements for the integration with the optical cavity. To tackle this problem we introduce a pipeline framework that allows us to produce transmon qubits with a frequency ranging between 8 GHz and 14 GHz in an efficient fashion. We also identify a promising hybrid 2D - 3D qubit control and readout platform and we simulate the complete system in detail.

This research work has been an amazing journey towards learning and discovery, at times demanding, but always exciting.

Part 1

# The effect of infrared light on superconducting circuits

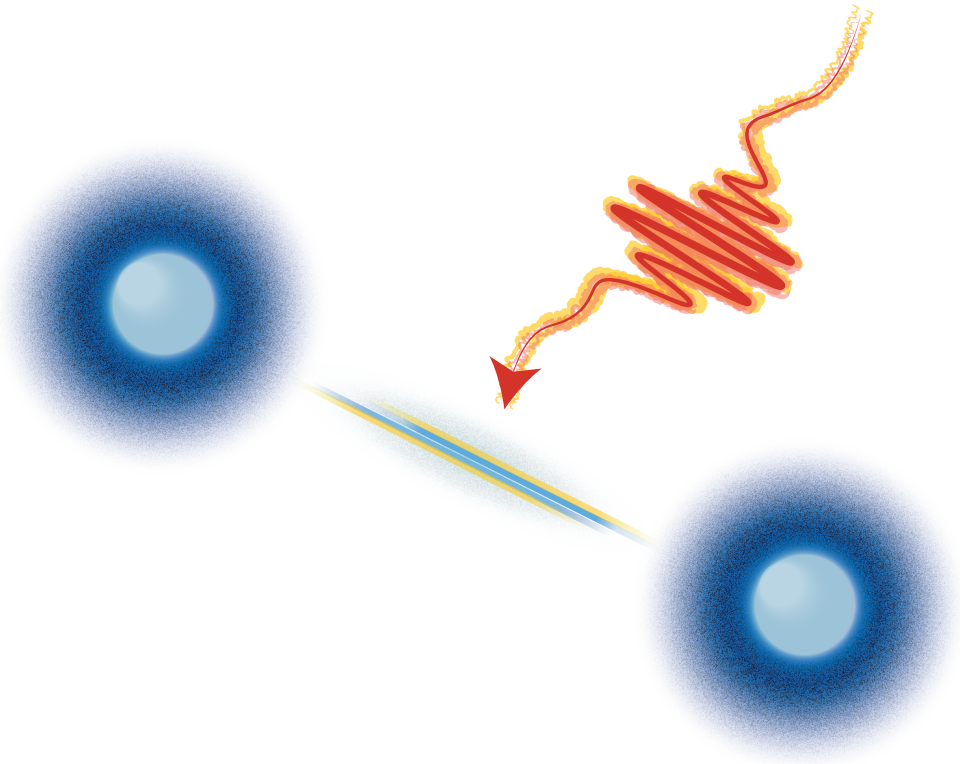

*"Science, in the act of solving problems, creates more of them."*
*A. Flexner*

Chapter 2

# Theoretical background

## 2.1. Quasiparticle dynamics

The interaction of IR light with a superconductor generates an intricate interplay among quasiparticles, Cooper pairs, phonons and photons. One of the main result of this process is a net decrease of superconductive electron pairs $n_{CP}$ and an increase in the number of quasiparticles $n_{qp}$, elementary excitations of the superconductors created when Cooper pair breaks apart [17]. This leads to a change in the resistive and inductive behavior of the superconductor. In the first part of this chapter we will introduce two different models describing the dynamic of quasiparticles generation and decay. The first model, derived during a previous project in the Hybrid Quantum Systems Group [18], is a one-dimensional diffusive model, considering the interplay between phonons, photons and quasiparticles. The second, derived by Wang et al. at Yale University [19], is a non-diffusive, non-spatial model, studying only the time evolution of quasiparticle density and introducing quasiparticle trapping by superconducting vortices.

### 2.1.1. 1D diffusive model

For the experiments discussed in this report the quasiparticle source is always well localized through the laser beam, shining on a limited region of the superconductor. At the beam spot IR photons directly break Cooper pairs and generate phonons by heating the superconductor and the substrate. These can still interact with superconducting electrons, breaking other Cooper pairs. The generated quasiparticles will then diffuse inside the material and eventually recombine into Cooper pairs by releasing new phonons.

This intricate process is studied more in detail in Ref. [18]. If we reduce the problem to one spatial dimension the main transport equations for quasiparticle and phonons could be written as [18]:

$$\frac{\partial n_{qp}(x,t)}{\partial t} = g(x,t) + \frac{2}{\tau_B} n_{ph}(x,t) - R n_{qp}(x,t)^2 + D\frac{\partial^2 n_{qp}}{\partial x^2} \tag{2.1}$$

$$\frac{\partial n_{ph}(x,t)}{\partial t} = R\frac{n_{qp}(x,t)^2}{2} - \frac{1}{\tau_B} n_{ph}(x,t) - \frac{1}{\tau_\gamma} n_{ph}(x,t) \tag{2.2}$$

with $n_{qp}$ and $n_{ph}$ respectively the quasiparticle and phonon densities, $D$ and $R$ the quasiparticles diffusion and recombination coefficients, $\tau_B$ the characteristic time for Cooper pair breaking by phonons, $\tau_\gamma$ phonon decay time due to other processes than

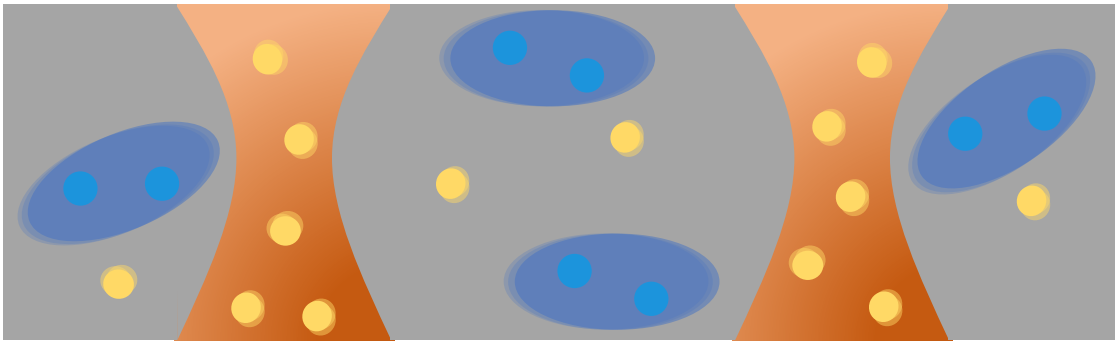

Figure 2.1.: Pictorial vortices representation in which quasiparticles can get trapped and decay.

Cooper pair breaking and $g(x,t)$ the quasiparticles generation term. Even if this model is accurately describing the interplay between quasiparticle, phonon and photons, a closed formula for $n_{qp}(x,t)$ is hard to obtain due to the complexity of the model.

### 2.1.2. Non-diffusive time evolution model

It is possible, through reasonable assumptions, to drastically simplify the model presented in equations (2.1), (2.2), and to achieve a closed formula describing the IR-generated quasiparticle time evolution.

Right after laser injection, recombination and diffusion will act to make the quasiparticle density constant across the superconductive region. After waiting sufficient time it could be possible to drop the diffusion term from equation(2.1) and to consider the density of quasiparticle constant $n_{qp}(x,t) = n_{qp}(t)$. As introduced in the previous section, it is also possible that phonons, generated by quasiparticle recombination, are still able to break other Cooper pairs, generating new quasiparticles. Following ref. [19], it is possible to include this effect in a lower recombination constant $r = r_{bare}/(F)$ with $F$ a factor in the range $5-10$ [19] and $r_{bare}$ the normalized 'bare' recombination constant for quasiparticles [19], and completely discard equation 2.2 .

The model from ref. [19] includes also the phenomenon of vortex quasiparticle trapping. In superconductors such as aluminum, the presence of an external magnetic field (even at mG levels) generates vortices, regions in which the magnetic field penetrates the superconductor and which are characterized by a lower superconductive gap. Quasiparticles can get trapped inside vortices and decay into Cooper pairs (Fig. 2.1).

With these assumptions the dynamic of quasiparticles density could be modeled as:

$$\frac{dx_{qp}}{dt} = -rx_{qp}^2 - sx_{qp} + g \tag{2.3}$$

with $x_{qp}$ the (spatially homogeneous) quasiparticle density normalized by the Cooper pair density ($n_{CP} \approx 4 \cdot 10^6\,\mu\text{m}^{-3}$ for aluminum [19]), $r$ and $s$ respectively the quasiparticle recombination and trapping rate and $g$ a generation term.

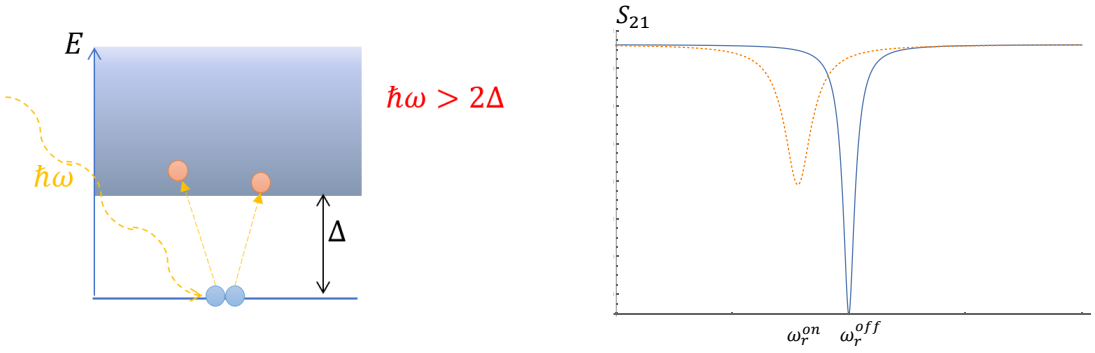


Figure 2.2.: **Left** Pictorial representation of IR photons breaking Cooper-pairs and generating quasiparticles. **Right** A theoretical plot of the resonator transmission spectrum $S_{21}$ obtained with (orange) and without (blue) IR-generated quasiparticles.

In this case, it is possible to obtain a closed formula describing the evolution of the normalized quasiparticle density $x_{qp}(t)$ after laser injection:

$$x_{qp}(t) = x^i_{qp} \frac{1 - r'}{e^{t/\tau_{ss}} - r'} + x^0_{qp} \tag{2.4}$$

with $\tau_{ss}$ a characteristic decay time, $0 < r' < 1$ a dimensionless fit parameter, $x^i_{qp}$ the initial injected quasiparticle density, $x^0_{qp}$ the steady state normalized quasiparticle density without injection from the laser.

From equation (2.3) it is possible to outline two different dominant behaviors for quasiparticle dynamics. In the case $sx_{qp} \gg rx^2_{qp}$ quasiparticles trapping will be the leading process, determining an exponential decay of $x_{qp}(t)$. In the case $sx_{qp} \ll rx^2_{qp}$ quasiparticle recombination will be dominant leading to an initially super-exponential decay of $x_{qp}(t)$.

## 2.2. Response of an electrical resonator to IR light

Superconducting resonators represent an easy and practical tool for investigating the interaction between IR laser light and superconductors. If we shine an IR laser beam on these devices it is possible to study the change in the frequency $\omega_i$ and internal quality factor $Q_i$ of the resonator to estimate the density of created quasiparticles $n_{qp}$ and study their time dynamics (Fig. 2.2). Moreover, it was already pointed out that the resonator photo-response depends on the current density $J_S$, with a higher resonator sensitivity if quasiparticles are created in a section where the current density is higher [20].

In the next sections we will introduce the main theoretical tools needed to understand how quasiparticles affect a superconducting resonator. We will start with a description of

the two-fluid model for superconductivity describing how quasiparticles and Cooper pairs affect superconductivity. We will use it to link the surface impedance of a superconductor to its kinetic inductance. We will then move to study the electrical resonator response to IR light. Indeed the generation of quasiparticles affect the London penetration depth, leading to a change of the superconductor surface impedance. This determines a variation of the kinetic inductance which is linked to the resonator frequency and quality factor. In this chapter we will introduce the hanger readout configuration and the circuit model of a resonator under IR laser illumination, following the analysis approach outlined in [21]. The key idea is to interact with the resonator through an input-output transmission line and study the transmission spectrum from the system. This will ultimately provide information on the quasiparticles density and its time evolution.

### 2.2.1. Two-fluid model for superconductivity

Different properties of a superconductor could be explained through a two-fluid model (Fig. 2.3) that postulates the coexistence of Cooper pairs and normal electrons inside a superconducting material [22]. The two fluids do not interact with eachother and give rise to two different behaviours. Below the superconducting critical temperature $T_c$ Cooper pairs can freely move without scattering with the lattice and they generate a resistance-free current. On the other hand, electrons display classic scattering processes inside the material. Processes such as electron-phonon, electron-electron or electron-impurity scattering will contribute to a finite restive component.

A simple description for the two fluid-model of superconductivity is based on Drude's model for electrical conduction. The formula for the alternating current (AC) conductivity $\sigma(\omega)$ is:

$$\sigma(\omega) = \frac{\sigma_{DC}}{1 + i\omega\tau} \tag{2.5}$$

with $\sigma_{DC}$ being the direct current (DC) conductivity, $\omega$ the angular frequency of the electric field and $\tau$ the scattering time. This formula outlines the presence of a resistive and inductive contribution associated to the carriers under analysis.

Electrons have generally a very short scattering time in metals. In the case of aluminum it is estimated that the electron scattering time at cryogenic temperature is around $\tau = 10^{-14} \sim 10^{-17}\, s$ [23]. This means that in the frequency regime $\omega/2\pi < 10\, GHz$, relevant for our project, Drude's conductivity for electrons could be considered as almost purely resistive:

$$\sigma_e(\omega) \approx \sigma_{DC} = \frac{n_e e^2 \tau}{m_e} \tag{2.6}$$

where $n_e$ is the density of electrons per unit volume, $\tau$ is electron scattering time, $e$ is the electric charge and $m_e$ the mass of the electron.

The situation is different for Cooper pairs. Below the superconducting critical current $I_C$ and magnetic field $B_C$ and for $T \ll T_C$ the relaxation time goes to infinity $\tau_{CP} \to \infty$. However, because of the absence of scattering, also the DC conductivity goes to infinity $\sigma_{DC} \to \infty$ and hence the ration $\sigma_{DC}/\omega\tau_{CP}$ remains finite. This results in a purely

inductive conductivity [20, 21]:

$$\sigma_{CP}(\omega) \approx -i\frac{2n_{CP}e^2}{m_e\omega} \tag{2.7}$$

with $n_{CP}$ the density of Cooper pairs. Even if Cooper pairs don't experience scattering, formula (2.7) highlights the fact that these particles posses an inertia that will oppose the change of current flow, resulting in an inductive component. The total Drude's model

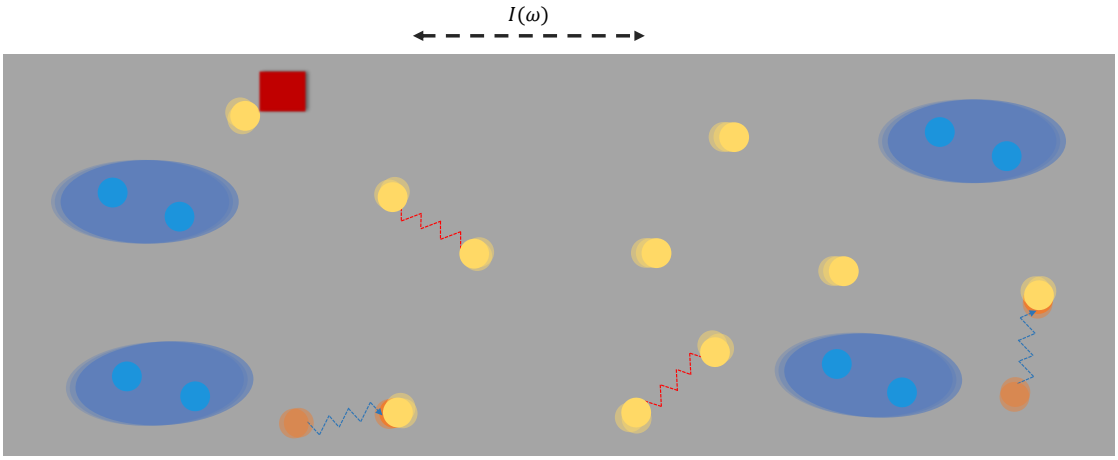


Figure 2.3.: Two-fluid model: Cooper pairs (blue) coexist with free electrons (yellow). It is possible to see a simple representation of electron-electron, electron-phonon (orange) and electron-impurity (represented by the red square) scattering events.

conductivity for a superconductor then becomes:

$$\sigma_{tot}(\omega) = \sigma_1 - i\sigma_2 = \frac{n_e e^2\tau}{m_e} + -i\frac{2n_{CP}e^2}{m_e\omega} \tag{2.8}$$

Note that, in the limit of DC current for $\omega \to 0$, $|\sigma_{tot}| \to \infty$, recovering the classical resistance free superconductive behavior. At $T < T_C$ in a superconductor almost all electrons will form Cooper pairs meaning that $n_{CP} \gg n_e$. As a result, formula (2.8) will have a strong inductive component and a small resistive one ($Re[\sigma_{tot}(\omega)] \ll Im[\sigma_{tot}(\omega)]$) In fact the conductivity of a superconductor at equilibrium is almost purely inductive and could be linked to the concept of surface impedance $Z_S = R_S + j\omega L_S$ to be introduced in section 2.2.3.

If we now consider a superconductive circuit element (such as an LC resonator), the presence of Cooper pairs will change the total inductance of the element [20]:

$$L_{tot} = L_{kin} + L_M \tag{2.9}$$

with $L_M$ the conventional magnetic inductance linked to the geometry of the circuit and

the magnetic permeability of the surrounding materials. The new contribution $L_{kin}$ is called *kinetic inductance* and it is representing the Cooper pair inductive contribution, as it will be explained in sec. 2.2.4. The complete system circuit schematic representation is shown in Fig. 2.4.

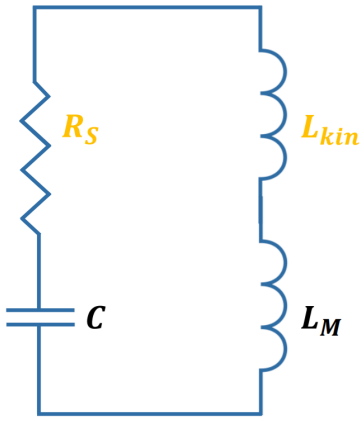


Figure 2.4.: Circuit structure of a LC superconductive resonator. The capacitance $C$ and the magnetic inductance $L_M$ are given by the circuit geometry. $R_S$ is associated to scattering electrons and $L_{kin}$ takes into account the inertia of Cooper pairs.

### 2.2.2. London penetration depth

In superconductors the London penetration depth is used to study the decay rate of the magnetic field inside a superconductor and it is defined as the depth at which the magnetic field is reduced by a factor of $e^{-1}$ w.r.t. its value at the surface. Supposing that we have an external magnetic field applied to the surface of a superconductor as sketched in Fig. 2.5 we can describe the magnetic field:

$$B(z) = B_0 \exp^{-z/\lambda_L(T)} . \tag{2.10}$$

The London penetration depth at a defined temperature $T$ can be written as [21]:

$$\lambda_L(t) = \sqrt{\frac{m_e}{2n_{CP}(T)e^2\mu_0}} = \frac{\lambda_L(0)}{\sqrt{1-(\frac{T}{T_C})^2}} \tag{2.11}$$

with $\mu_0$ the magnetic permeability and $\lambda_L(0)$ defined as:

$$\lambda_L(0) = \sqrt{\frac{m_e}{2n_{CP}(0)e^2\mu_0}} \tag{2.12}$$

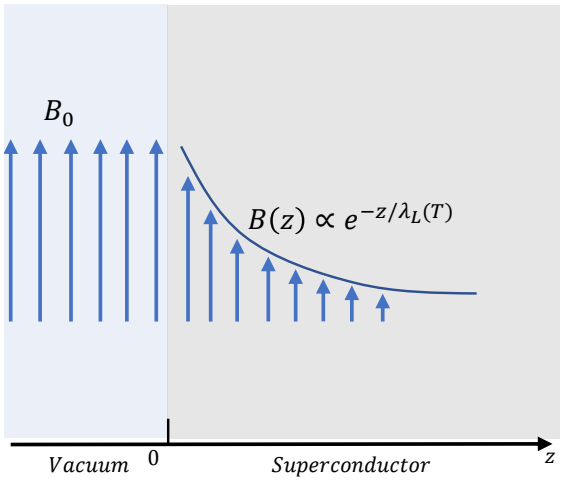


Figure 2.5.: Behavior of an incident magnetic field on a superconductor (gray) coming from vacuum (light blue)

The temperature dependence of the Cooper pair density $n_C P(T)$ can be approximated as:

$$n_{CP}(T) = n_{CP}(0)\left(1 - \left(\frac{T}{T_C}\right)^m\right) \tag{2.13}$$

with m an approximate exponent ranging between 2, in the case of thin films $\lambda_L(T) \gg w$, to 4 in the case of thick films $\lambda_L(T) \ll w$, with $w$ the thickness of the superconductive layer [24]. In our case, with $w \sim 80\,\text{nm}$ and $\lambda_L \sim 15\,\text{nm}$ for aluminum, a good value for m is 4 .

### 2.2.3. Surface Impedance

The interaction of electromagnetic fields with a metal or a superconductor could be studied using the concept of surface impedance. Consider an x-polarized electromagnetic wave which is normally incident on the surface of a superconductor. The surface impedance $Z_s$ is defined as [25]:

$$Z_s = \frac{E_x}{H_y}\Big|_{z=0} \tag{2.14}$$

where $E_x$ and $H_y$ are respectively the total electric and magnetic field at the surface in a system of reference where the $x$ and $y$ axis are oriented according to the EM field directions (Fig. 2.6). As shown in ref. [25] it is possible to write the surface impedance as:

$$Z_s = \sqrt{\frac{i\omega\mu_0}{\sigma(\omega)}} \tag{2.15}$$

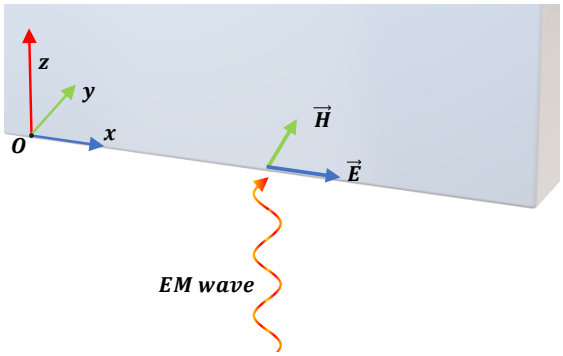


Figure 2.6.: Picture of an electromagnetic (EM) wave normally incident on the surface of a superconductor (gray).

Combining equation (2.15) and (2.8) we obtain the following approximated formula [26]:

$$Z_s = R_S + i\omega L_s = \frac{1}{2}\omega^2\mu_0^2\lambda_L(T)\sigma_1 + i\omega\mu_0\lambda_L(T). \tag{2.16}$$

with $L_S = \mu_0\lambda_L(T)$

### 2.2.4. Linking surface and kinetic inductance

In order to understand the connection between kinetic inductance and surface inductance, consider a layer of superconductive material of length $l$ and a superconductive current density $\vec{J_s}$ flowing through it (Fig. 2.7). Let us also suppose that the current density could be approximated as constant throughout the cross-section.

The current flow implies that Cooper pairs will have some kinetic energy that could be computed as [21]:

$$K_{CP} = \int_V \frac{2m_e n_{CP} \vec{v_{CP}}^2}{2} dV = \frac{m_e}{4n_{CP}e^2}\int_V \vec{J_s}^2 dV = \frac{1}{2}\frac{m_e}{2n_{CP}e^2}\frac{l}{A}I^2 = \frac{1}{2}L_{kin}I^2 \tag{2.17}$$

$$\vec{J_s} = -2en_{CP}\vec{v_{CP}} \tag{2.18}$$

with $\vec{v_{CP}}$ the velocity of Cooper pairs travelling inside the lattice, $A$ the area orthogonal to current direction and $L_{kin}$ the kinetic inductance that can be written as:

$$L_{kin} = \frac{m_e}{2n_{CP}e^2}\frac{l}{A} \tag{2.19}$$

If we suppose that the current is generated by an normally incident EM wave on the surface of the superconductor and that the thickness of the layer $t$ is much bigger than the London penetration depth ($t \gg \lambda_L(T)$) we would have that the current is actually only generated in a thin section of our superconductive layer. In particular $A = \lambda_L(T)w$

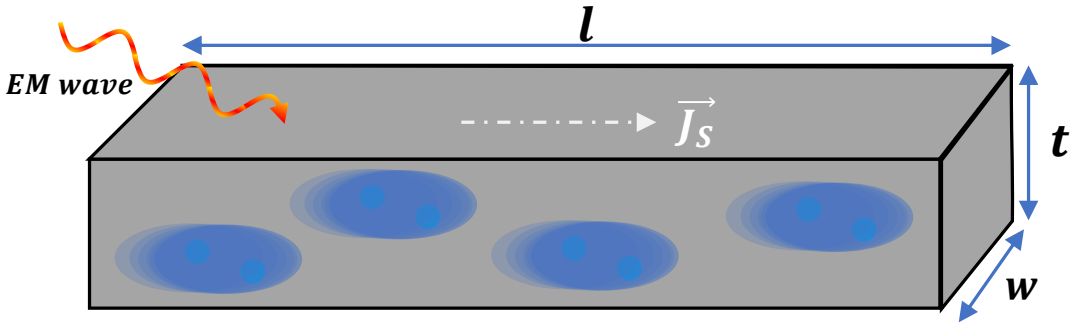


Figure 2.7.: Graphical representation of a superconductive material with a superconducting current $\vec{J}_s$ flowing through it. The current is generated by an incident EM wave.

with $w$ the width of the superconductive section. This implies that:

$$L_{kin} = \frac{m_e}{2n_{CP}e^2\lambda_L(T)}\frac{l}{w} = \mu_0\frac{\lambda_L(T)^2}{\lambda_L(T)}\frac{l}{w} = \mu_0\lambda_L(T)^2\frac{l}{w} = L_s\frac{l}{w} \tag{2.20}$$

Formula (2.20) shows that the kinetic inductance is a directly linked to the surface inductance of a superconductor.

### 2.2.5. Resonator characterization

In our experiments the resonator will be coupled capacitively to an input-output line. Through the study of the reflection and transmission parameters $S_{11}$ , $S_{21}$ it is possible to extract the internal resonator quality factor $Q_i$ and its resonance frequency $\omega_0$. These quantities provide information about $L_{kin}$ and $Z_s$ and hence about the quasiparticle density $n_{qp}$, as it will be explained in subsection 2.2.6.

A first possible readout configuration is the *reflection* configuration showed in Fig. 2.8. The input signal is routed towards the resonator and the reflected signal is redirected to the output line through the use of a circulator. The resonator has internal losses, modeled through $\kappa_i$ and the coupling to the in-out line is represented by $\kappa_c$. The response of the resonator is described by using input-output theory, from which the following transmission coefficient can be derived [27]:

$$S_{21}^{refl}(\omega) = \frac{i(\omega-\omega_0)+\kappa_c-\kappa_{tot}}{i(\omega-\omega_0)-\kappa_{tot}/2} \tag{2.21}$$

with $\kappa_{tot} = \kappa_i + \kappa_c$ .

Another possible configuration is the *hanger* configuration (Fig. 2.8). In this case the readout resonator is simply capacitively coupled to the input output line. The transmis-

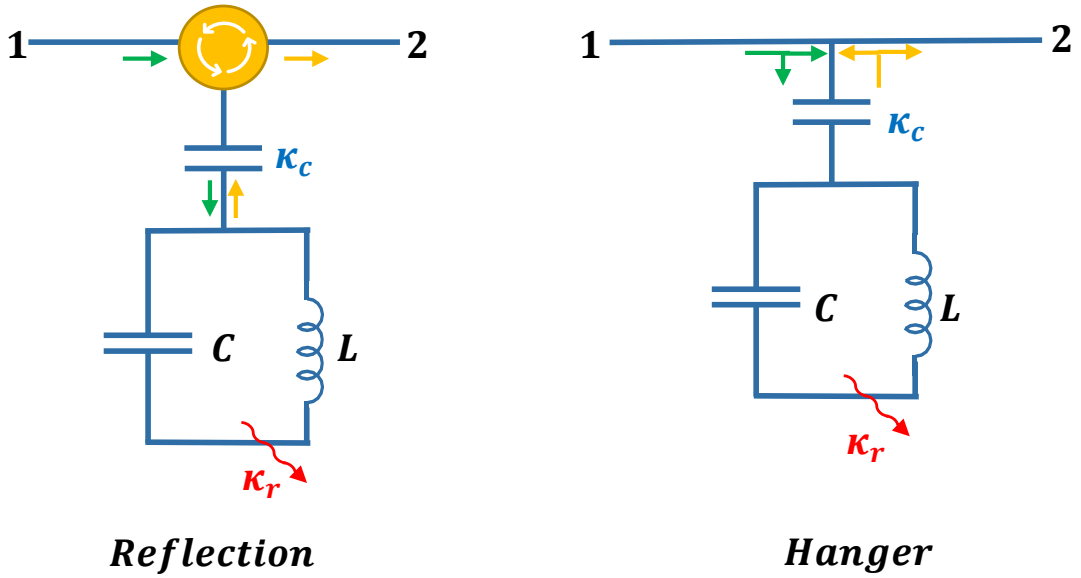


Figure 2.8.: The *reflection* (right) and *hanger* (left) configurations.The circulator is represented in yellow and the arrows represent the incoming (green) and reflected power (orange). Notice that in the *hanger* configuration part of the input power goes directly from *port 1* to *port 2* and part of the reflected power reaches *port 1*.

sion coefficient could be derived as [27]:

$$S_{21}^{hang}(\omega) = \frac{1}{2}(1 + S_{21}^{refl}(\omega)) = \frac{i(\omega - \omega_0) - \kappa_i/2}{i(\omega - \omega_0) - \kappa_{tot}/2} \tag{2.22}$$

This configuration is the one used for performing our experiments, as it does not require any external element (such as the circulator in the reflection measurement), avoiding attenuation from other circuit elements.

### 2.2.6. Circuit model of a resonator under IR light

The circuit of an LC superconductive resonator is sketched in Fig. 2.4. The circuit features a capacitive and inductive component $C$, $L_m$ linked to the geometry of the element, a kinetic inductance $L_{kin}$ and a resistance $R_S$ induced by the surface impedance $Z_S$ as previously introduced. By inspection of the electrical circuit we could derive the equation of motion [21]:

$$\ddot{I} + \frac{R_S}{L_m + L_{kin}}\dot{I} + \frac{1}{(L_m + L_{kin})C}I = 0 \tag{2.23}$$

$$\ddot{I} + \kappa_i \dot{I} + \omega_0^2 I = 0 \tag{2.24}$$

In the case of the IR laser interacting with an LC resonator the loss rate $\kappa_i$ and the resonance frequency $\omega_0$ will be affected by a change in the quantities $R_S$ and $L_{kin}$.

Starting from formula (2.16) it is possible to define $R_S$ as:

$$R_S = \frac{1}{2}\frac{l}{w}\omega^2\mu_0^2\lambda_L^3(T)\frac{n_{qp}e^2\tau}{m_e} \tag{2.25}$$

with $\tau$ the electron scattering time, $l$ and $w$ respectively the width and the length of the resonator. Using the formula of the kinetic inductance from equation (2.19), and equation (2.11) we get:

$$\kappa_i = \frac{R_S}{L_m + L_{kin}} = \frac{\frac{1}{2}\frac{l}{w}\omega^2\mu_0^2\frac{(n-2n_{CP})e^2\tau}{m_e}(\frac{m_e}{2n_{CP}(T)e^2\mu_0})^{3/2}}{L_m + \mu_0(\frac{m_e}{2n_{CP}(T)e^2\mu_0})^{1/2}} \tag{2.26}$$

$$\kappa_i = \frac{\frac{1}{2}\frac{l}{w}\omega^2\frac{(n-2n_{CP})\tau}{2n_{CP}(T)}(\frac{\mu_0 m_e}{2n_{CP}(T)e^2})^{1/2}}{L_m + \mu_0(\frac{m_e}{2n_{CP}(T)e^2\mu_0})^{1/2}} \tag{2.27}$$

with $n$ the volume density of electrons at room temperature, $\mu_0$ the vacuum magnetic permeability and $\omega \approx \omega_0$ in our case. The density of quasiparticles is given by the difference between the total electron and the Cooper pairs electron density $n_{qp} = n - 2n_{CP}$. However, this formula holds only in the case of an uniform quasiparticle distribution across all the superconductor. If we have a localised quasiparticle source, as in the case of a laser beam shining on the device, supposing small changes in the number of Cooper pairs and considering timescales much shorter than the quasiparticles diffusion time, we can refer to the following formula [21]:

$$\frac{\Delta\kappa_i}{\kappa_i} = -\frac{\Delta n_{CP}(3n - 2n_{CP})}{2n_{CP}(n - 2n_{CP})}F_{laser} \tag{2.28}$$

with

$$F_{laser} = \frac{\int f_{laser}(x,y)J^2 dxdy}{\int J^2 dxdy} \tag{2.29}$$

with J(x,y) the current density function, $\Delta n_{CP}$ the average density of Cooper pairs broken by laser beam, and $f(x,y)$ a function which has the same intensity profile of the laser power but it is normalized $\int f_{laser}(x,y)dxdy = 1$. This formula is not directly derived from equation(2.27), but it is obtained starting from the definition of energy loss rate as $\kappa_i = \frac{PowerLoss}{EnergyStored}$ [21]. It is also worth noticing that $F_{laser}$ could be seen as analogous to the participation ratio for the laser light.

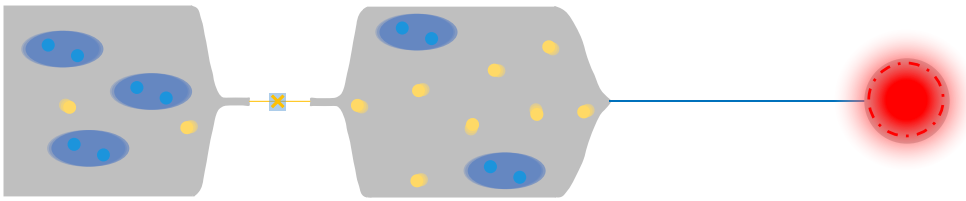

Figure 2.9.: Graphical representation of the qubit under IR Illumination. The laser (red) illuminates the antenna side and it generates quasiparticles (yellow) by breaking Cooper pairs (blue). Quasiparticles can then diffuse towards the Josephson junction.

## 2.3. Response of a transmon qubit to IR light

In the context of the optomechanical transduction experiment it is essential to estimate the direct effect of IR-generated quasiparticle on superconducting qubits. The poisoning effect of quasiparticles on superconducting qubits has been object of study since the introduction of the Cooper pair box [28]. In superconducting qubits based on Josephson junctions the tunneling of quasiparticles changes the charge parity of the junction electrodes and modifies the excess charge on qubit islands [28]. Moreover this process induces coupling to the phase across the junction generating unwanted qubit excitations or de-excitations [16]. In a transmon, it is predicted that both the dephasing and unwanted (de)excitations rate due to parity switching should be exponentially suppressed in $-\sqrt{8E_J/E_C}$, $E_J$ and $E_C$ being respectively the Josephson and charging energy [16]. However many experiments have shown that, even in a transmon, quasiparticles tunneling could visibly affect qubit lifetime and coherence time [19, 29, 30].

In the context of optomechanical transduction it is hence essential to estimate the direct effect of IR-generated quasiparticles as this could bound the efficiency and the success rate of the transduction process itself.

### 2.3.1. Effect of quasiparticles on the decay rate

As previously introduced quasiparticles can generate unwanted (de)excitations and dramatically affect qubit decay rate. A very straightforward formula to estimate this effect

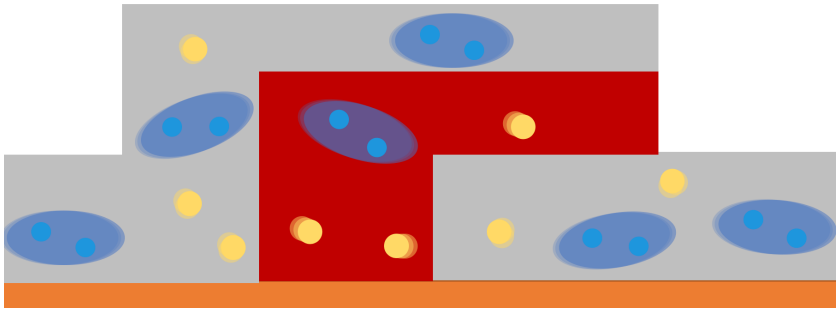

Figure 2.10.: Representation of the Josephson junction. It is possible to see the 2 superconducting layers (gray) separated by an insulating layer (red). Cooper pairs (blue) and quasiparticles (yellow) tunneling through the junction. Quasiparticles tunneling can generate uncontrolled (de)excitations and increase qubit decoherence.

is given by [19]:

$$\Gamma_1(t) = Cx_{qp}(t) + \Gamma_1^{ex} \tag{2.30}$$

where $x_{qp} = n_{qp}/n_{cp}$ the quasiparticle densities near the Josephson junction normalised by the Cooper-pair density ($n_{cp} \approx 4 * 10^6 \mu m^{-3}$ in aluminum [19]), $\Gamma_1^{ex}$ the qubit decay rate in absence of IR-generated quasiparticles and

$$C = \sqrt{2\omega_q \Delta/\pi^2 \hbar}$$

with $\omega_q$ the qubit frequency and $\Delta$ the superconducting gap. Notice that we could then use the decay rate to measure the injected quasiparticle density near the Josephson junction evolving in time.

In our experiment the quasiparticle source is well localized through the laser beam, shining on the qubit antenna, at a distance $d \approx 1000\,\mu m$ from the Josephson junction. At the beam spot IR photons can directly break Cooper pairs or generate phonons by heating the substrate. These can also interact with superconducting electrons breaking other Cooper pairs. The generated quasiparticles will then diffuse towards the junction, affecting qubit performances.

This intricate process could be studied using the model presented in section 2.1.1. The transmon qubit showed in Fig. 2.9 under IR illumination is reduced to a one dimensional model. In our case, for a Gaussian beam laser that is pulsed on for a time $\Delta t_{laser}$, our generation term can be written as:

$$g(x,t) = g_0 \frac{e^{\frac{(x-x_0)^2}{2\sigma^2}}}{\sqrt{2\pi\sigma^2}} [\Theta(t) - \Theta(t - \Delta t_{laser})] \tag{2.31}$$

with $x_0$ the peak position of the laser beam in this 1-d model, $\sigma$ the laser beam waist, $\Theta(t)$ the temporal Heaviside function and $g_0$ a generation term taking into account the

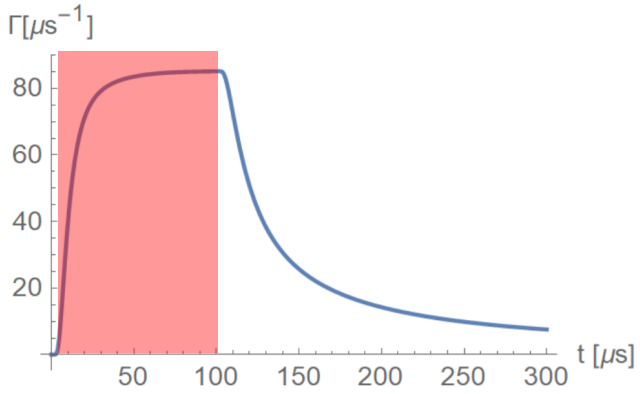


Figure 2.11.: Qubit decay rate evolution w.r.t. time. The region in red indicates when the laser pulse is on. It is possible to see an initial increase, due to quasiparticles diffusion towards the junction, a saturation and then a decay after the laser pulse and quasiparticles recombination. Picture taken from [18].

partial absorption of the total laser power.

Using realistic parameters [18] it is possible to compute the change of the decay rate of the qubit with respect to time. The result is shown in Fig. 2.11.

Unfortunately, as previously stated in section 2.1.1, due to the non-linearity of the model, it is impossible to obtain a closed formula for the evolution of $\Gamma_1(t)$. This becomes possible, however, if the model presented in section 2.1.2 is instead adopted. In this case, using equation (2.30), it is possible to compute the evolution of the qubit decay rate as a function of time:

$$\Gamma_1(t) = C x^i_{qp} \frac{1 - r'}{e^{t/\tau_{ss}} - r'} + \Gamma^0_1 \tag{2.32}$$

with $C$ defined as in (2.30), $0 < r' < 1$ a dimensionless fit parameter, $x_i$ the initial injected quasiparticle density, $\Gamma^0_1 = C x^0_{qp} + \Gamma^{ex}_1$ and $x^0_{qp}$ respectively the qubit relaxation rate and the quasiparticle normalised density without quasiparticle injection from the laser.

As previously introduced in sec. 2.1.2 it is possible to observe an exponential decay of $\Gamma_1(t)$ in the case $s \gg r$ and an super-exponential one in the case $s \ll r$ (Fig. 2.12).

### Qubit frequency shift due to quasiparticles

Quasiparticles do not simply affect the qubit lifetime but their influence could be observed also in the shift of qubit frequency $\omega$. As described in [19] it is possible to link the quasiparticle-influenced qubit decay rate to the qubit frequency:

$$\delta\omega = -\frac{1}{2}(\Gamma_1 - \Gamma^0_1)\left[1 + \pi\sqrt{\frac{\hbar\omega}{2\Delta}}\right] \tag{2.33}$$

It is interesting to notice that a frequency shift, varying in time, will induce an additional qubit dephasing, affecting the qubit dephasing rate $\Gamma_2$.

## 2.4. Superconducting resonator vs transmon qubit

In previous sections we have analyzed the effect of IR-generated quasiparticles on a superconducting resonator and a transmon qubit.

It is worth noticing that studying the qubit $\Gamma_1$ provides only information about the quasiparticle density $n_{qp}$ localized near the Josephson junction. On the other side, the resonator $\kappa_i$ and $\omega_r$ are affected by the global quasiparticle density. These differences should give rise to alternative responses of the resonator and of the qubit to laser light.

Moreover, while $\Gamma_1 \propto n_{qp}$ is always approximately true for the quasiparticles density near the junction, $\kappa_i \propto n_{qp}$ and $\omega_r \propto n_{qp}$ holds only for really small quasiparticles densities.

It is also likely that, when shining the laser pulse on the qubit antenna (as shown in Fig. 2.9), there will be some 'dead time' between the end of the pulse and the peak response in the qubit $\Gamma_1$ (Fig.2.11), due to quasiparticle diffusion time. For the resonator, conversely, we should see an almost instantaneous response.

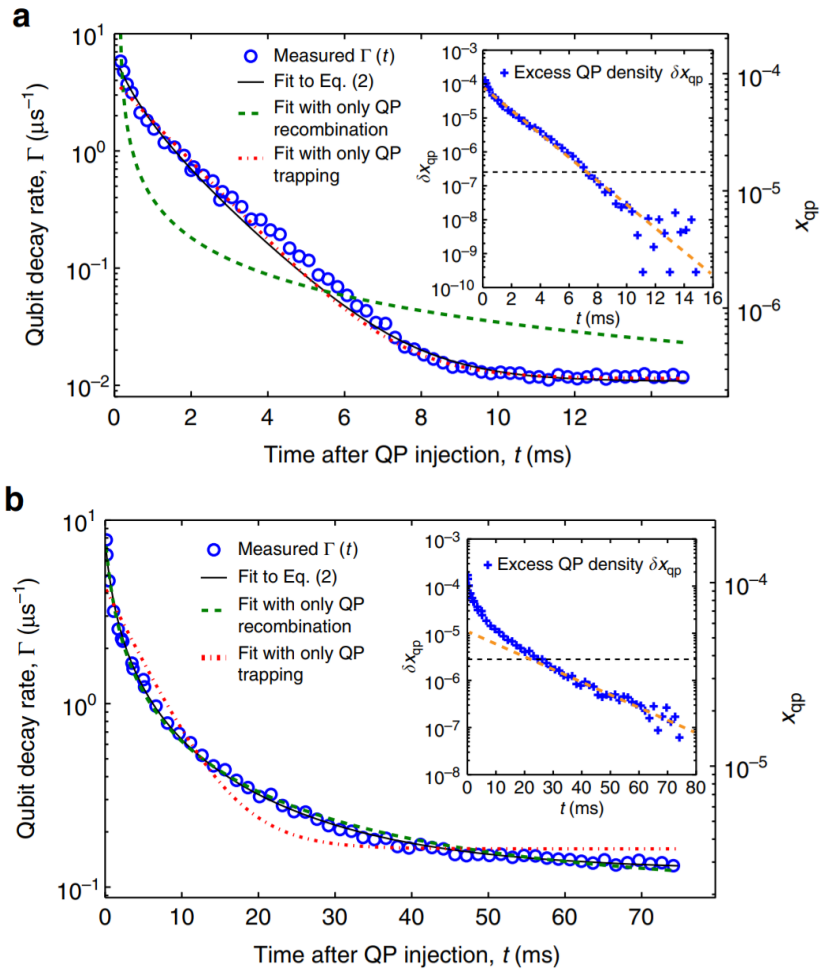


Figure 2.12.: **a)** Qubit decay rate in the case of quasiparticles trapping. The evolution of $\Gamma_1$ in this case follow an exponential law. The inset shows also the quasiparticle density $x_{qp}$ with respect to time, extracted from $\Gamma_1$.
**b)** Qubit decay rate in the case of quasiparticles recombination. The evolution of $\Gamma_1$ in this case follow a super-exponential law. The inset shows also the quasiparticle density $x_{qp}$ with respect to time, extracted from $\Gamma_1$. Reproduced from Ref. [19].

Chapter 3

# Experimental Setup

As previously introduced, one of the two main goals of this project is to investigate the interaction between IR light and superconducting devices. Fig. 3.1 identifies the main clusters composing the experimental setup. In order to render quantum effects visible and suppress thermal noise the device under test (DUT) is housed inside a dilution refrigerator at a temperature $T \approx 10$ mK. A laser source is generating IR light that is then sent to the DUT through an optical fiber. Microwave electronic GHz signals are also routed towards the sample from outside the refrigerator and they are used to control and read the state of the superconducting device. In next sections a more accurate analysis of each single setup cluster will be presented.

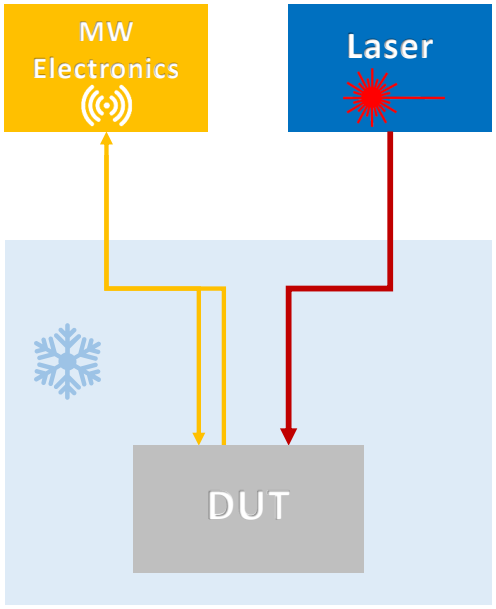


Figure 3.1.: Sketch of the clusters composing the experimental setup.

## 3.1. Laser control setup

The laser setup controls the shape, intensity and timing of the IR pulses sent to the superconducting device. The setup is depicted in Fig. 3.2. Laser light at a wavelength

$\lambda = 1550$ nm is continuously generated by a laser source (Pure photonics PPCL500) and is then fed to an acousto-optic modulator (AOM Brimrose TEM-150-18-30-1580-2FP), with an extinction ratio of more than 50 dB and a rise time of around 30 ns. This device is able to diffract and shift the frequency of incoming light by using sound waves at radio-frequency (Fig. 3.3). The AOM takes as input the incoming laser light and a pre-amplified arbitrary MW pulse, modulated at a frequency $f_{mod} = 150$MHz, generated by Quantum Machines Operator X (OPX) and produces a laser pulse with the same shape as the MW pulse. This also causes a change in laser frequency by the same 150 MHz, which is however not relevant to this experiment. After being sent to the fridge and interacting with the DUT, a small part of the incoming light is collected by a fiber collimator, whose main role is to route as much power as possible far from the mixing chamber. A photodiode then detects the incoming light and sends the data to the measurement PC.

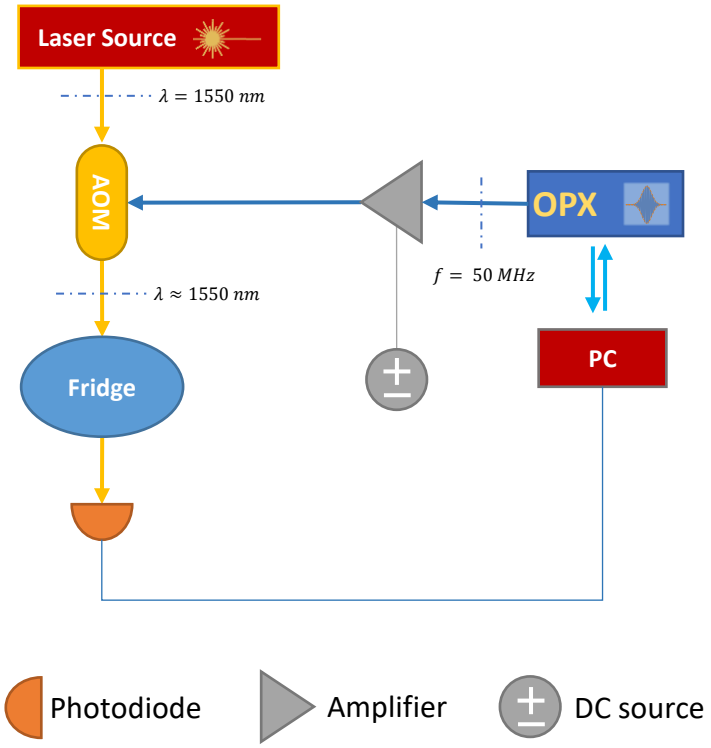


Figure 3.2.: Laser control setup.

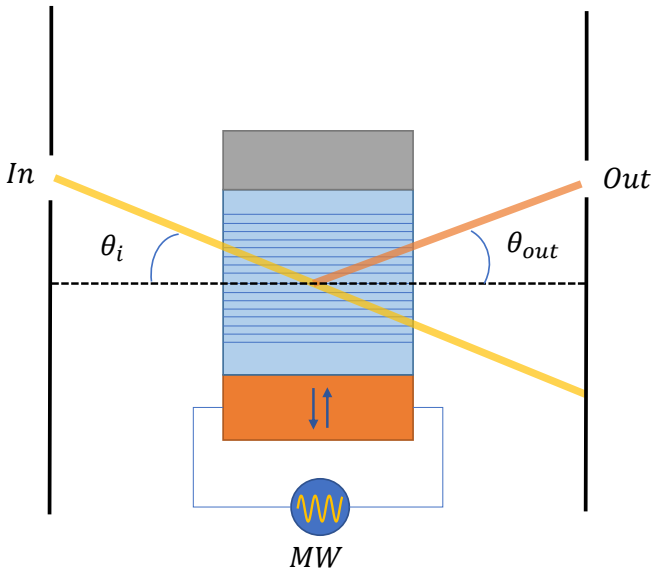


Figure 3.3.: Schematic representation of an acousto optic modulator. A microwave frequency (MW) signal is applied to a piezoelectric substrate (orange) and the stress induced by the electric field generate vibrations inside a material like glass or quartz (blue). The incoming laser beam (yellow) is partially diffracted (orange) changing the beam angle w.r.t. to the normal axes of the crystal from $\theta_i$ to $\theta_{out}$. The device is designed such as that only the diffracted beam is able to reach the output port.

## 3.2. Microwave setup

### 3.2.1. Resonator readout setup

The interaction of IR-generated quasiparticles with an electrical resonator could be analyzed through the change in the resonator quality factor $Q_r$ and resonance frequency $\omega_r$. As previously discussed, these parameters can be extracted by studying the transmission spectrum $S_{21}(\omega)$ of the resonator in the Hanger configuration. Fig. 3.4 represents the simple setup adopted to reach this goal. A Vector Network Analyzer (VNA) is connected to a measurement PC, in order to setup the measurement and collect the data. The VNA receives triggers from the OPX, synchronizing measurements with laser pulses. At each laser pulse the VNA performs a single point measurements of the spectrum $S_{21}(\omega)$, by sending a MW pulse to the fridge with a power of $-50\,\mathrm{dBm}$, measured at the output of the VNA.

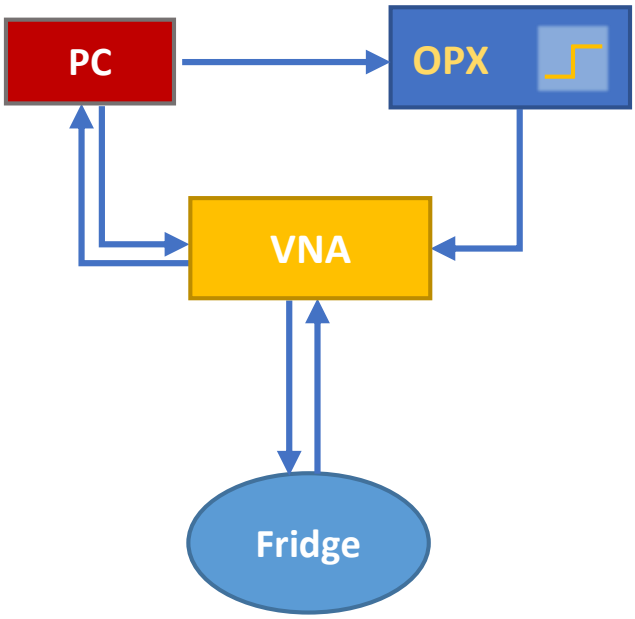


Figure 3.4.: Resonator readout circuit.

### 3.2.2. Qubit control and readout setup

As previously introduced, the effect of quasiparticles acting on the qubit could be studied through the evolution of the qubit decay rate w.r.t. time $\Gamma(t)$. This requires the ability to reliably excite and readout the state of the qubit.
When building a qubit control and readout setup it is important to consider that this system is composed by a transmon qubit and by a cavity readout resonator. The circuit should be able to directly interact with the qubit only when performing state control operations, while it should interact with the cavity resonator for performing state readout, in order to avoid fast state decay.

The complete circuit is showed in Fig. 3.5. The qubit control signal is generated by the OPX in the form of I and Q quadratures at a frequency $f_I = f_Q = 50\,\text{MHz}$ and up-converted with an IQ microwave mixer (Marki IQ0618LXP) through a local oscillator source (RF 1- Windfreak), delivering a signal at a frequency $f_{RF\,1} \approx f_{qubit} \approx 5$ GHz. The IQ up-conversion scheme is replicated also for the qubit readout signal. In this case, the only difference lies in the frequency of the local oscillator (RF 2- Marki IQ4509LXP), from Rohde & Schwarz, which will be $f_{RF\,2} \approx f_{cavity} \approx 9$ GHz. The output of both mixers is then is forwarded to a combiner that is able to merge the qubit control and readout signals. The result is then fed to a 10 dB directional coupler, that samples a small amount of the input power (-10 dB) and sends it to a Spectrum Analyzer connected to the measurement PC. This is done to be able to perform the proper calibration of both the IQ mixers. The signal then reaches the fridge and interacts with the DUT. The

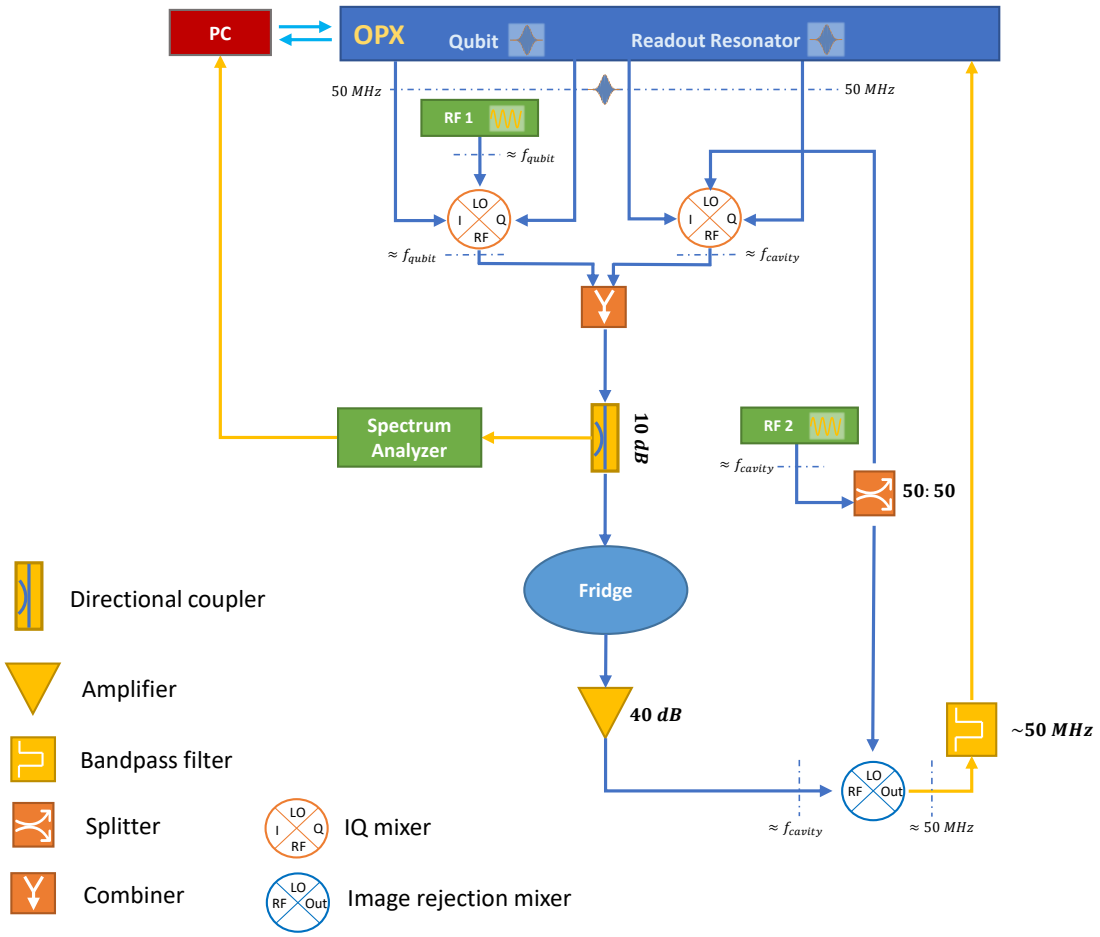


Figure 3.5.: Qubit Readout and control circuit.

transmitted signal exits the dilution refrigerator and is then amplified again with a 40-dB room-temperature amplifier (AmpliTech APT4-04001200-1510-D4). An image rejection mixer(Marki IRW0618LLXW-1), is used to down-convert the amplifier output by mixing it with the LO achieving a final signal frequency $f_{out} \approx 50\,\text{MHz}$. To reduce spurious noise as much as possible the signal goes through a band-pass filter and it finally reaches the input channel of the OPX to be analyzed.

## 3.3. Inside the fridge

At the last stage of the dilution refrigerator we find the device under test. A 3D CAD representation is showed in Fig. 3.6.

The laser light coming from the optical fiber is focused using a GRIN lens (n. 64-531) from Edmund Optics. The lens is hosted in a Thorlabs Polaris Mount (POLARIS-K05F6), a tilting mount stable at cryogenic temperatures. The beam is directed toward a MW Cavity and it is focused either on the superconducting device with a previously adjusted beam waist of $51\,\mu m$ (measured w.r.t. an intensity drop of $1/e^2$). After the cavity a fiber collimator, housed in a custom mount, collects a part of the transmitted light into a multimode fiber (Thorlabs - FG105LCA) that is routed outside the fridge. The multimode fiber and collimator were chosen to maximize collection NA for minimal heating of the base stage. All the components are mounted on a custom bracket that ensures a reproducible laser alignment.

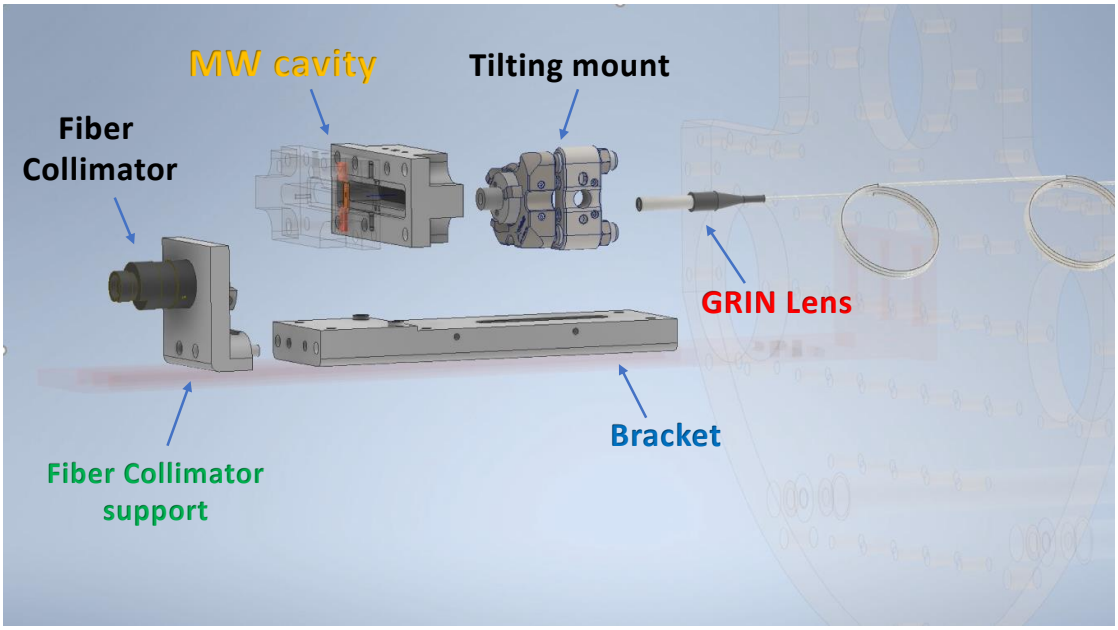


Figure 3.6.: Exploded 3D CAD representation of the device under test. In this case the MW qubit cavity is shown but this could be interchanged with the resonator tunnel.

More details about this section can be found in appendix A.

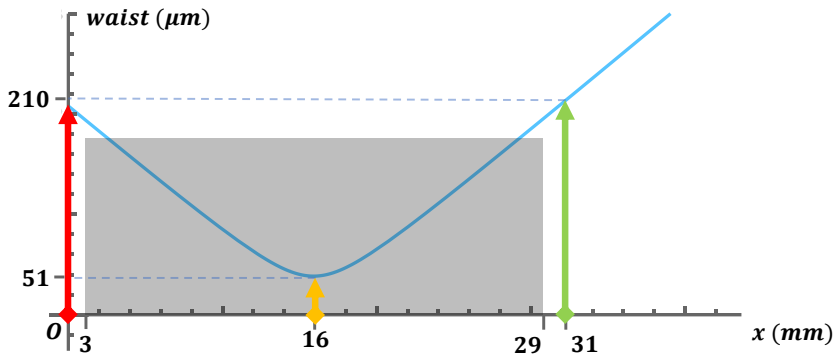


Figure 3.7.: Evolution of the beam diameter through the system. The end face of the GRIN lens is represented by the red arrow, the sample by the yellow arrow and the fiber collimator front face by the green arrow. The Gaussian beam profile is in blue, and the outline of the MW cavity is in gray.

Chapter 4

# Dipstick Experiment

Studying the interaction between infrared (IR) laser photons and superconducting Cooper Pairs poses many challenges. Among those is an accurate determination of the laser beam position. Indeed, simple alignment at room temperature does not suffice as, during the cooldown, thermal contraction of the Polaris Mount relative to the other components on the bracket (described in section 3.3) can drastically modify the final beam position. Moreover the Fiber collimator (see appendix A.3), a promising candidate for collecting the light that was not absorbed or reflected by the DUT, was never tested at cryogenic temperatures. In this regime the performances of the collimator could be dramatically affected, preventing the device from working efficiently. It was hence necessary to perform a complete characterisation of the collimator at cryogenic temperatures.

In order to address these challenges,we used a simple setup to rapidly cool the experiment by immersion in liquid nitrogen (from here on referred to as the 'dipstick'). Even if the final temperature reachable with this device is $\sim 77$ K instead of $\sim$ mK as in the case of the dilution refrigerator, we expect thermal contractions to be strongest at the high temperatures, as most thermal expansion coefficients decrease exponentially with temperature. In this chapter we provide an analysis on the fiber collimator efficiency and on the Polaris Mount misalignment at low temperatures.

## 4.1. Fiber collimator characterisation

The setup used for testing the collimator is shown in Fig. 4.1. The fiber collimator and Polaris mount were mounted inside the dipstick in an optimal alignment position to guarantee a maximal transmission. During each cooldown IR laser light is sent to the Polaris mount, which holds a graded index (GRIN) lens to focus the beam from the fiber at a spot $16.03 \pm 0.1$ mm in front of the lens facet. This beam is collected by the fiber collimator and sent to a photo-diode through a multi-mode fiber, allowing us to monitor the collected power (transmission) change with respect to temperature. Fig. 4.2 shows a characteristic curve obtained in the process, highlighting a dramatic drop in the collection efficiency. In the cooldown from $\sim 300$ K to $\sim 100$ K the transmission drop is around 50% . Moreover for temperatures lower than $\sim 100$ K the collection efficiency oscillates around a constant average value, rendering very hard to find final precise value. Eight cooldowns were performed to gain statistics and, using the transmission data collected in the last $\sim 5$ K of the cooldown, we obtained the histogram showed in Fig. 4.2. The

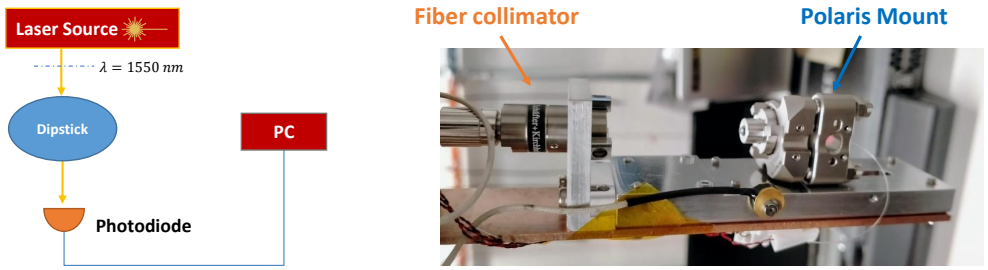


Figure 4.1.: **Left** The experimental setup used to study the collimator performances. **Right** The Polaris mount and the fiber collimator mounted inside the dipstick.

average collection efficiency from this data is:

$$\eta = 0.51 \pm 0.027.$$

## 4.2. Misalignment test

In order to study the response of superconducting devices to IR light it would be favorable to asses the position of the laser beam relative to the DUT as precisely as possible inside the fridge. At room temperature, through the use of the IR microscope, it is possible to adjust the IR beam position with $\mu m$ precision. However at cryogenic temperatures the thermal contractions of materials could lead to the misalignment of the beam and dramatically affect light absorption from our device and hence its response to infrared quasiparticles. Using the dipstick it was possible to study the Polaris Mount misalignment, characterizing separately the vertical and horizontal laser shift with respect to the sample.

### 4.2.1. Horizontal misalignment

The setup we used is shown in Fig. 4.3. The Polaris mount shines light towards electrical resonator which is hosted inside the resonator tunnel. The laser beam, hitting one of resonator pads is partially shadowed by it and this limits the power that the fiber collimator collects from the beam itself.

Before cooling down the device, a calibration curve is taken, showing the power dependence with respect to the laser position relative to the resonator pad (Fig. 4.4). The beam is moved in the horizontal direction, by using the Polaris mount actuator. The actuator displacement is measured using a custom angle measurement tool designed for

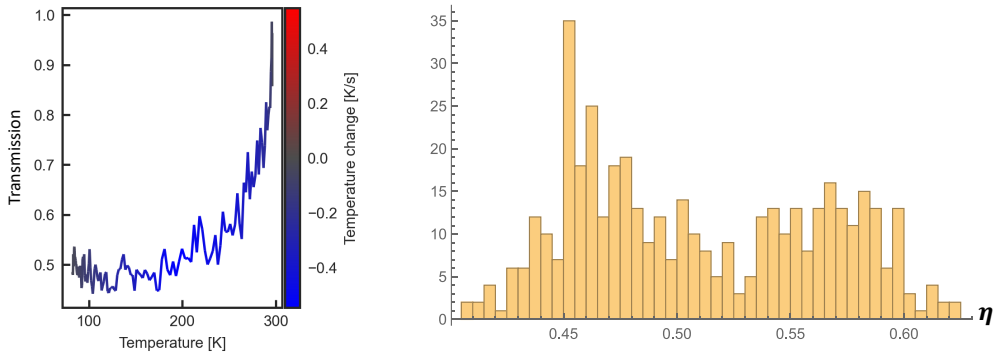


Figure 4.2.: **Left** cooldown curve showing the trend of the transmission with respect to the measured temperatures. **Right** Histograms presenting the measured values of the collimator efficiency,, collected during eight cooldowns from all data points between 82 and 77K.

the experiment, able to measure the angle rotation $\theta_x$ of hexagonal key controlling the actuator. FIG. 4.4 shows the power change with respect to the angle movement. As the angle increases, the beam moves towards the resonator and it is partially blocked by it, decreasing the power collected by the collimator. The power profile should follow the functional form:

$$P_x(\theta_x) = \frac{1}{\sqrt{2\pi\sigma^2}} \int_{-\infty}^{\infty} e^{\frac{-(u-\theta_x)^2}{2\sigma^2}} S(u-\theta_{x0})\, du \tag{4.1}$$

with $\mu$ and $\sigma$ respectively the beam central position and variance, $\theta_{x0}$ the position of the edge of the resonator on the x axis measured with the custom angle tool, and $S(\theta_x)$ a 1D step function. It is worth noticing that in this case we assumed the laser beam profile to be Gaussian.

Once the calibration curve is ready a high-sensitivity working point is selected, i.e. on the steep part of the slope of this curve. In this particular case an initial angle of $\theta_{x_i} = 80\,^\circ$ was chosen with a corresponding initial power $P_i$. The device is then cooled down and the power collected by the fiber collimator is constantly monitored through the photodiode. Once at the final temperature $T_f \approx 77$ K is reached it is possible to measure the final power correcting also for the fiber collimator loss in performances

$$P_{x_f} = \frac{P^m_{x_f}}{\eta}$$

with $P^m_f$ the measured power and $\eta$ the fiber collimator efficiency at cryogenic temperatures. We then invert the curve $P_x(\theta_x)$ obtaining the final angle $\theta_{x_f}$ reached by the Polaris mount and the corresponding angle shift $\Delta\theta_x$. This procedures is repeated two times (Fig. 4.5) propagating the error associated to the collimator efficiency $\eta$. The final

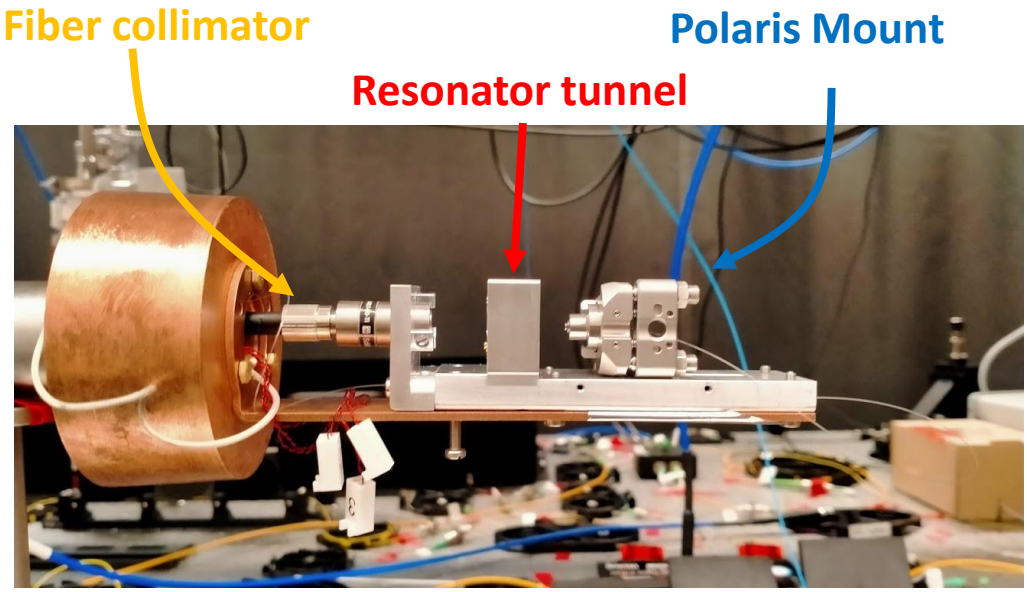


Figure 4.3.: In order to measure the horizontal Polaris mount misalignment, a resonator chip hosted inside a tunnel is added to the setup at the beam waist.

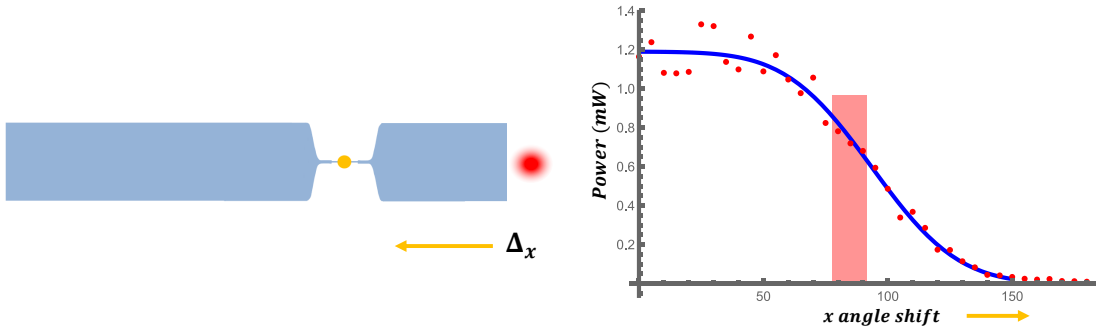


Figure 4.4.: **Left** Representation of the relative position of the laser beam with respect to the resonator. **Right** Calibration curve showing the change of power with respect to the horizontal beam movement. The arrow in orange shows the correspondence between beam movement and increase of $\theta y$.

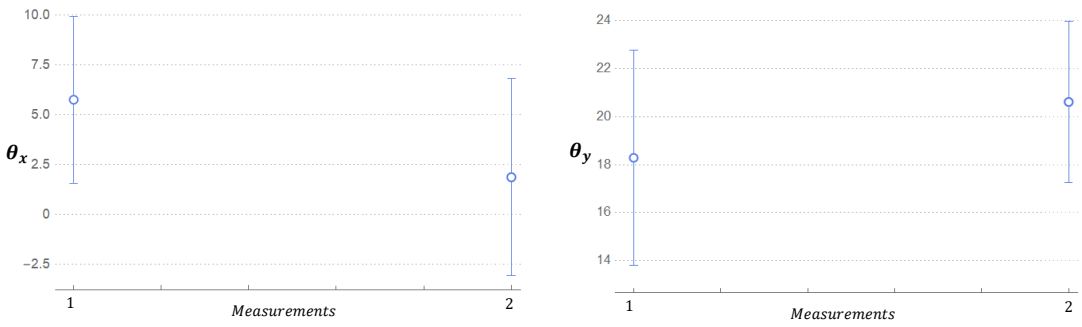


Figure 4.5.: **Left** Values of $\Delta\theta_x$ measured in two different cooldowns. **Right** Values of $\Delta\theta_y$ measured in two different cooldowns. In both cases we see that the uncertainty bars of the the two measurements intersect.

obtained average angle shift is

$$\Delta\theta_x = \theta_{x_f} - \theta_{x_i} = 19.45 \pm 1.9\,^\circ,$$

corresponding to an approximate shift in the x direction of

$$\Delta x = 12.75 \pm 1.28\,\mu\text{m}.$$

The conversion from angle to position is approximate and it is obtained by measuring the movement of the laser beam relative to the resonator chip using the IR microscope (sec. A.4). Knowing the microscope magnification and camera pixel size, we can convert a observed displacement on the camera to an actual displacement of the beam focus. It is worth noticing that the angle shift is the quantity used for correcting the Polaris mount misalignment. The imprecision on the angle-position shift conversion is then not relevant.

### 4.2.2. Vertical misalignment

A similar procedure was repeated for calibrating vertical misalignment. In this case one of the qubit pads was used as it offered a good horizontal translational invariance. The procedure followed was similar to the one outlined in the previous section. A calibration curve was obtained, describing $P_y(\theta_y)$, the power dependence with respect to the vertical angle shift $\theta_y$ (Fig. 4.6).

We cool down with an initial angle of $\theta_{y_i}$ and we measure the corrected power collected by the collimator $P_{y_f}$. By reversing the fitted power is then possible to obtain the final angle $\theta_{y_f}$ and the related angle shift $\Delta\theta_y$. We repeat this measurement two times and

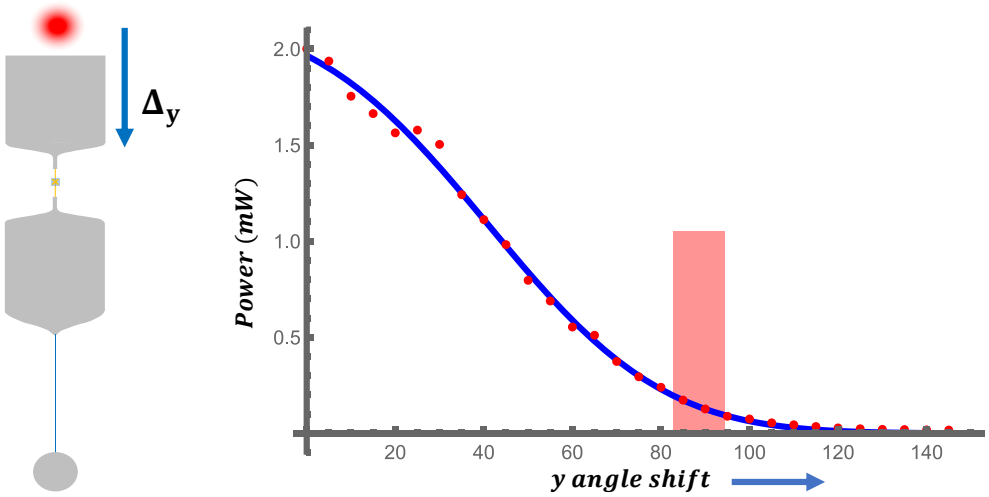


Figure 4.6.: **Left** The laser beam position relative to the qubit chip. **Right** Calibration curve showing the change of power with respect to the vertical beam movement. The arrow in blue shows the correspondence between beam movement and increase of $\theta x$.

we obtain a final average angle shift (Fig. 4.5):

$$\Delta\theta_y = \theta_{y_f} - \theta_{y_i} = 3.82 \pm 2.28\,^\circ,$$

corresponding to $y$ shift of

$$\Delta y = 2.43 \pm 1.47\ \mu\text{m}.$$

It is here worth noticing that the misalignment $\Delta y$ is almost negligible while the misalignment $\Delta x$ direction accounts for a shift of more than 10 % of the laser beam waist $w = 102\,\mu$m.

### 4.2.3. Correcting the misalignment

With the obtained values for vertical and horizontal misalignment $\Delta\theta_y$ and $\Delta\theta_x$ it is possible to correct for laser thermal misalignment. We start with the laser beam at the wanted position, corresponding to the vertical and horizontal angles $\theta_y^i$ and $\theta_x^i$. We then compensate for the thermal angle shift by moving the laser beam position of $-\Delta\theta_y$ and $-\Delta\theta_x$ achieving the final corrected angle positions:

$$\theta_y^{corr} = \theta_y^i - \Delta\theta_y\,,$$

$$\theta_x^{corr} = \theta_x^i - \Delta\theta_x\,.$$

During the cooldown, the laser beam angle changes will be approximately equal to the ones introduced in the corrected angle position achieving a final angle position:

$$\theta_y^f = \theta_y^{corr} + \Delta\theta_y^{cd} \approx \theta_y^i \,,$$

$$\theta_x^f = \theta_x^{corr} + \Delta\theta_x^{cd} \approx \theta_x^i$$

with $\Delta\theta_y^{cd}$ and $\Delta\theta_x^{cd}$ respectively the real vertical and horizontal angle shifts during the cooldown.

### 4.2.4. Testing the misalignment corrections

We performed a simple test to verify the correctness of the misalignment data. We first aligned the laser beam on the resonator circular pad, we then intentionally misaligned it (Fig. 4.7) of $-\Delta\theta_x$ and $-\Delta\theta_y$ , and we cooled the device into liquid nitrogen. Unfortunately, the diffraction of the laser beam on the circular pad of the resonator generated interference inside the multimode fiber connected to the fiber collimator. This caused strong oscillations of collected power and thus prevented obtaining reliable data and to measure whether the effect of the intentional misalignment was effectively correcting the Polaris mount thermal misalignment.
Despite the test not being successful we decided to use the collected data for pre-correcting laser misalignment before putting the device inside the fridge. Indeed, even a partial compensation of the laser thermal shift is beneficial.

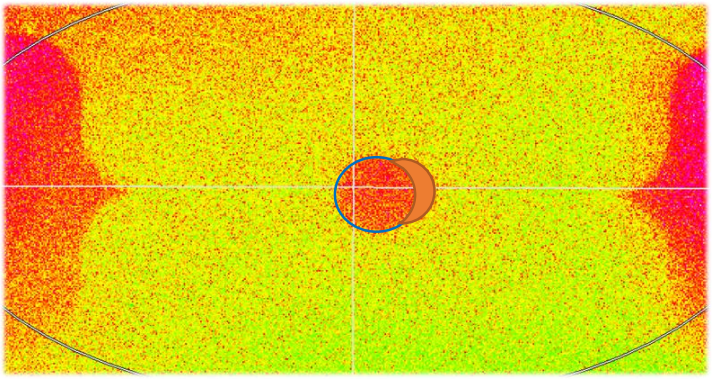

Figure 4.7.: IR microscope image showing the resonator circular pad (blue circle) and part of the laser beam (red full circle) that was intentionally misaligned to compensate for the Polaris mount thermal misalignment during cooldown. This was also done before mounting the sample inside the dilution fridge.

Chapter 5

# Electrical resonator experiment

As previously introduced, the electrical resonator represents a practical and promising platform for the study of the interaction of IR light with superconducting devices. In this chapter we will present a detailed description of the resonator experiment. After presenting the main measurement sequence and fitting analysis we will introduce an experiment studying the influence of thermalization time on sample heating. In the following section we investigate the time dynamic of the resonator response to IR laser pulse and we study the response of the resonator to a wide range of laser pulse energies. We then conclude the chapter with some final discussion on the implications of the collected data for the microwave to optic transduction experiment.

## 5.1. Time sequence

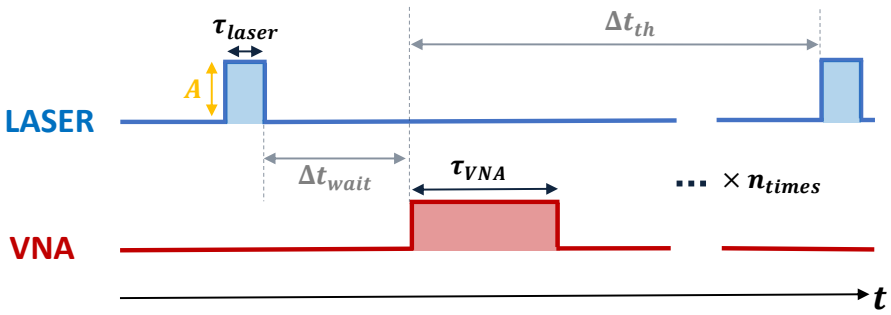


Figure 5.1.: Time sequence representation. In this case $n_{times} = n_{av} \times n_{pt}$.

To properly perform the interaction experiment each VNA measurement should be precisely synchronized with laser pulse emission. Fig. 5.1 illustrates the measurement sequence adopted. A square laser pulse is produced through the AOM, with an arbitrary pulse length $\tau_{laser}$ and AOM amplitude $A$, measured in Volts. After a waiting time $\Delta t_{wait}$ the VNA measurement is started by a trigger signal from the OPX. The measurement takes a time $\tau_{VNA}$, depending on the required frequency resolution. After starting the

VNA measurement we finally wait a thermalization time $\Delta t_{th}$ to let the sample thermalize with the mixing chamber stage. As the VNA acquires only a single frequency point during the measurement time $\tau_{VNA}$ the sequence is repeated $n_{pt}$ to acquire a single complete transmission spectrum of the resonator $S_{21}(\omega)$. Each spectrum is then collected a $n_{av}$ times. Table 5.1 shows the characteristic value of each presented quantity.

| | |
|---|---|
| $\tau_{laser}$ | $100\,ns$ |
| $\Delta t_{wait}$ | $10 - 10000\,\mu s$ |
| $\tau_{VNA}$ | $100 - 1\,\mu s$ |
| $\Delta t_{th}$ | $1 - 30\,ms$ |
| $A$ | $0 - 0.3\,V$ |
| $n_{av}$ | $10^2 - 10^3$ |
| $n_{pt}$ | $10^2 - 10^4$ |

Table 5.1.: Characteristic values of each important experiment quantity.

## 5.2. Fitting routine

As introduced in previous chapters, through the VNA it is possible to measure the transmission spectrum $S_{21}$ of the resonator in the Hanger configuration. The final formula reads [31]:

$$S_{21} = Ce^{i\psi}\left(1 + e^{i\phi}\frac{2i(\omega - \omega_r) - \kappa_c + \kappa_i}{2i(\omega - \omega_r) + \kappa_c + \kappa_i}\right) \tag{5.1}$$

with $\kappa_c$ and $\kappa_i$ respectively the resonator in-out line coupling rate and resonator internal loss rate, $\omega_r$ the resonator frequency, $C$ a re-scaling constant, $\psi$ and $\phi$ different phase offsets acquired by the signal along the readout line. It is important to point out that for the quasiparticle analysis the only parameters of interests are $\omega_r$ ,$\kappa_i$.

After collecting experimental data from the VNA, it is possible to use standard fitting routines such as the Levenberg–Marquardt algorithm to fit it. A spectrum example, taken when the laser is off, is shown in Fig. 5.2 and the fitted parameters are shown in Table 5.2 .

## 5.3. Thermalization time

As previously introduced the thermalization time is the time needed by the sample to thermalize with the mixing chamber stage. It is an important factor for the experiment as, by repeating the sequence thousands of times, it is essential not to progressively heat the sample. On the other hand, a long thermalization time implies a low experiment repetition rate, affecting the time required for performing the experiment. It was then important to find a 'sweet spot' for the thermalization time to speed up the experiment without generating residual heat in the sample.

| | Fit result | Simulated |
|---|---|---|
| $\omega_r/2\pi$ | $4.378 \pm 42 \cdot 10^{-9}$ GHz | 4.35 GHz |
| $\kappa_c/2\pi$ | 100 kHz | 128 kHz |
| $\kappa_i/2\pi$ | $27.4 \pm 0.05$ kHz | – |

Table 5.2.: Table showing the fitted parameters from a resonator spectrum with the laser off. It is possible to see also the simulated values obtained in the project design phase. We simulated the resonator, the tunnel cavity hosting it and the readout pin using Ansys HFSS. The simulation results gave us an estimation of the resonator frequency and coupling to the readout line shown in the table.

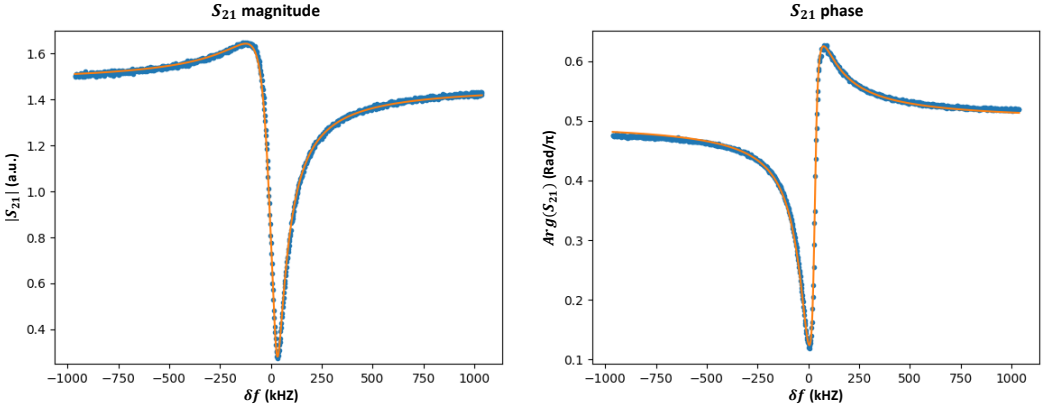


Figure 5.2.: Amplitude and phase of the transmission spectrum when the laser is off. The x axis displays the frequency shift from the resonator frequency when laser is off $\delta f = f - \omega_r^{off}/2\pi$. Data points are shown in blue and corresponding fitted curves in orange.

To reach this aim a single point of the resonator spectrum $|S_{21}(\omega_{min})|$ corresponding to the minimum of the transmission spectrum, was repeatedly measured while reducing thermalization time $\Delta t_{th}$. The result is shown in Fig. 5.3. For a thermalization time $\Delta t_{th} > 1\,ms$ we observe no heating. In view of this result we chose a thermalization time $5\,ms < \Delta t_{th} < 10\,ms$ for all our experiments.

## 5.4. Time dynamics

The second experiment studies the time evolution of quasiparticles through the effect on the resonator internal loss rate $\kappa_i$ and resonance frequency $\omega_r$. A constant laser power before the AOM and AOM voltage (both are set independently) and laser pulse length were chosen, determining a fixed laser pulse energy

$$E_{laser} = P_{laser} \cdot \tau_{laser}$$

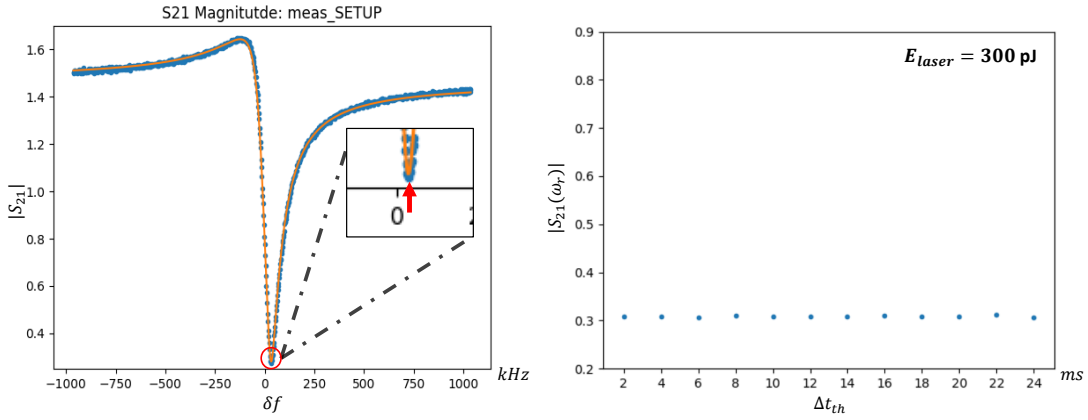


Figure 5.3.: **Left** The spectrum of the resonator when the laser is off. The inset is showing the point (red arrow) that was repeatedly measured for the experiment. **Right** The $|S_{21}(\omega_{min})|$ value with respect to the thermalization time $\Delta t_{th}$. In this case $P_{laser} = 600\,\mu$W and $\tau_{laser} = 500\,$ns.

with $P_{laser}$ the laser power at the mixing chamber and delivered to the sample and $\tau_{laser}$ the pulse time length. The measurement time of the VNA was also fixed and the chosen values are reported in Table 5.3. A time analysis was performed, by sweeping the waiting time $\Delta t_{wait}$.

| | |
|---|---|
| $P_{laser}$ | $600\,\mu W$ |
| $\tau_{laser}$ | $500\,ns$ |
| $E_{laser}$ | $300\,pJ$ |
| $\tau_{VNA}$ | $50\,\mu s$ |

Table 5.3.: Experiment parameters. Notice that $P_{laser}$ and $E_{laser}$ are respectively the power and the energy arriving at the mixing chamber and delivered to the sample.

Fig. 5.4 shows a color plot of the inverse-modulus and phase of $S_{21}(\omega, t)$, the resonator transmission spectrum, evolving in time. Fig. 5.5 shows also the spectra obtained at $\Delta t_{wait} = 0\,\mu s$ and at $\Delta t_{wait} = 1\,ms$ when the effect of laser-generated quasiparticles is not visible anymore. By a quick qualitative analysis of the spectra it is clear that the laser pulse is causing a negative frequency shift $\delta\omega_r < 0$ and an increase of the internal loss rate $\delta\kappa_i > 0$.

Using the fitting routine described in section 5.2 it was possible to extract all the unknown parameters of equation (5.1) from experimental data. In the next section a particular focus was placed on the time evolution of $\kappa_i$ and $\omega_r$

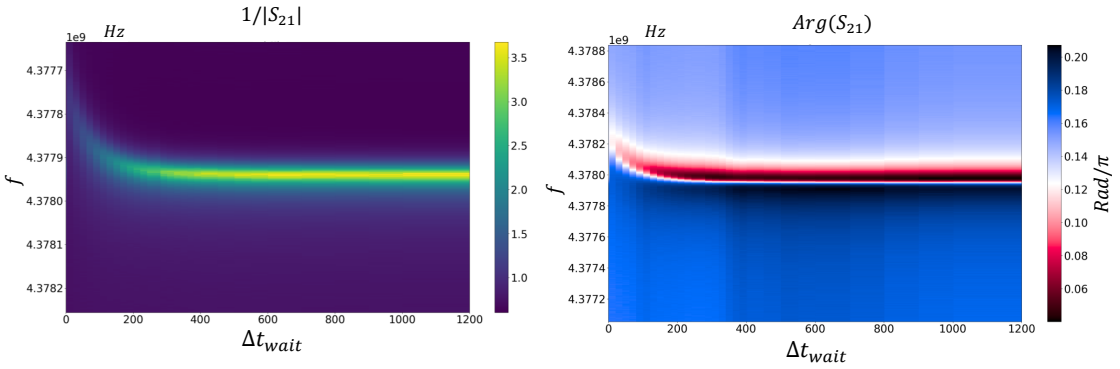


Figure 5.4.: Inverse modulus (**Left**) and phase (**Right**) of the transmission resonator spectrum. In the modulus plot it easy to follow the motion in time of the resonator $1/|S_{21}|$ maximum (the dip in the modulus of the resonator spectrum $|S_{21}|$). The dip position moves in frequency and its value grows as the delay time $\Delta t_{wait}$ increases, highlighting a frequency shift $\omega_r$ and a decrease of the resonator loss rate $\kappa_i$ as quasiparticles recombine into Cooper Pairs.

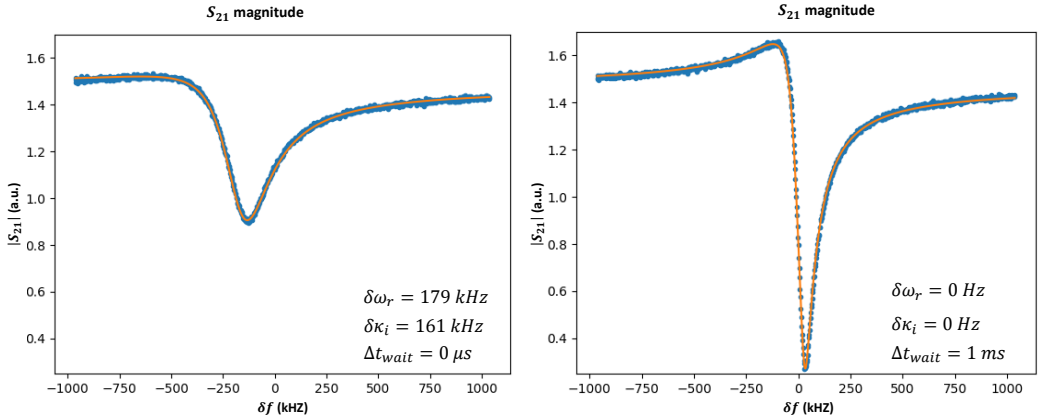


Figure 5.5.: Modulus of the resonator transmission spectrum at $\Delta t_{wait} = 0\,\mu s$ (**Left**) and at $\Delta t_{wait} = 1\,ms$ (**Right**).

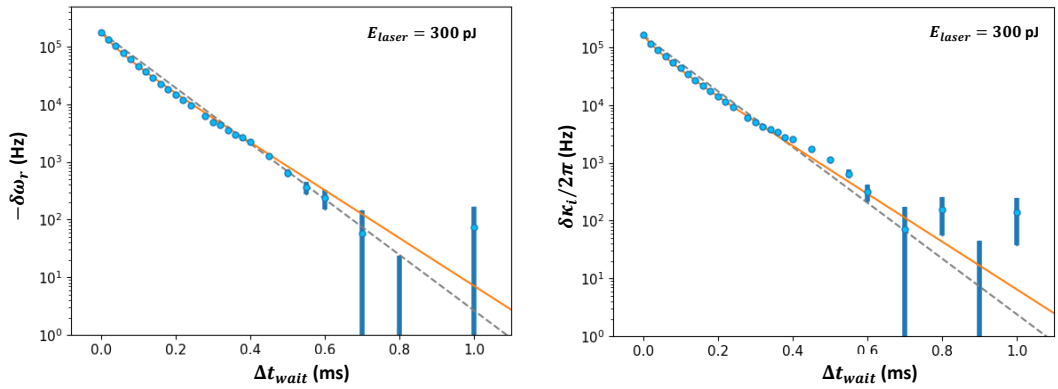


Figure 5.6.: Time evolution of the extracted resonator frequency $\delta\omega_r/2\pi$ (**left**) and linewidth $\delta\kappa_i/2\pi$ (**right**) change for a measurement with a laser pulse energy $E_{laser}$ of 300 pJ. Data points are shown in blue with $1\sigma$ error-bar and the fitting curves of equations (5.2) and (5.3) are shown in orange. In gray we show a simple exponential decay fit. In this case $P_{laser} = 600\,\mu$W and $\tau_{laser} = 500\,$ns.

### 5.4.1. $\kappa_i$ and $\omega_r$ time evolution

From the non-diffusive time evolution model presented in section 2.1.2 the normalized quasiparticle time evolution could be described using equation (2.4). The model did not consider quasiparticles spatial diffusion and neglected completely any phonon-quasiparticle dynamics. In our experiment, however, the laser beam is generating quasiparticles in a localized region of the superconductor, inevitably leading to quasiparticle diffusion across the resonator. Despite this different experimental condition it is possible to use equation (2.4) to fit the time evolution of the internal loss rate $\kappa_i(t)$ and of the frequency of the resonator $\omega_r(t)$. The adapted fitting equations become:

$$\kappa_i(t)/2\pi = A_1^{\kappa_i}\frac{1-r'}{e^{t/\tau_{ss}}-r'} + A_0^{\kappa_i} \tag{5.2}$$

$$\omega_r(t)/2\pi = A_1^{\omega_r}\frac{1-r'}{e^{t/\tau_{ss}}-r'} + A_0^{\omega_r} \tag{5.3}$$

It is worth noticing that, even if a fitting is possible using equations (5.2) and (5.3), the violation of the underlying experimental assumptions means that the fitted parameters can not be interpreted the way they are intended to be. The implications of this will be further discussed in section 5.4.2.

Fig. 5.6 shows the extracted $\kappa_i(t)$ and $\omega_r(t)$ collected data with the fitting curve with the parameters outlined in Table 5.4.

This data is consistent with the notion that $\kappa_i(t)$ and $\omega_r(t)$ are proportional to the

| | $A_1$ (Hz) | $A_0$ (Hz) | $\tau_{ss}$ ($\mu$s) | $r'$ |
|---|---|---|---|---|
| $\kappa_i/2\pi$ | $1.614 \cdot 10^5$ | $2.734 \cdot 10^4$ | 105 | 0.45 |
| $\omega_r/2\pi$ | $-1.786 \cdot 10^5$ | $4.378 \cdot 10^9$ | 105 | 0.45 |

Table 5.4.: Fitted values for the parameters in equations (5.2) and (5.3).

normalised quasiparticle density $x_{qp}(t)$. We explain the direct proportionality between of $\kappa_i(t)$ and $\omega_r(t)$ with $x_{qp}(t)$ supposing that the laser-generated density of quasiparticle is still much smaller than the density of Cooper Pairs $\delta x_{qp} \ll 1$. In this regime it is then possible that

$$\delta\omega_r \propto -\delta x_{qp}$$

and

$$\delta\kappa_i \propto \delta x_{qp}.$$

Moreover equation (2.4) describes quasiparticle decaying through trapping and recombination. The same assumptions were at the basis of the analysis in ref. [19]. However we note that our results could also be explained by a model that considers quasiparticle recombination and diffusion from the illuminated resonator pad across the superconductor.

### 5.4.2. Interpreting the time dynamics

From the value of $r'$ shown in Table 5.4 it is possible to see that both quasiparticles trapping 2.1.2 and recombination are roughly equally relevant processes, leading to a super-exponential decay for $\kappa_i$ and $\omega_r$. The weak residual magnetic field inside the fridge determines a non-zero vortex density in the superconductor, probably explaining the reason for the residual trapping behaviour.

From the theory developed in section 2.1.2 it would be expected that the value of $r'$ and $\tau_{ss}$ remain constant with respect to a change in the number of quasiparticles injected $x^i_{qp}$. To test this hypothesis we performed additional $\kappa_i$ and $\omega_r$ time analysis, while lowering the laser power $P_{laser}$ and fixing $\tau_{laser}$. The results are collected in Table 5.5.

| $E_{laser}$ ($pJ$) | $\tau_{ss}$ ($\mu s$) | $r'$ |
|---|---|---|
| 300 | 105 | 0.45 |
| 30 | 190 | 0.75 |
| 3 | 400 | 0.95 |

Table 5.5.: Table showing the fitted $r'$ and $\tau_{ss}$ parameters for different $E_{laser}$.

This shows that our hypothesis was not confirmed by preliminary data. The change in laser pulse energy $E_{laser}$ causes large variability in the parameters $\tau_{ss}$ and $r'$. The reason for this phenomenon is still not understood and it is also worth noticing that, in the case $E_{laser} = 3\,pJ$, the quality of the fit (5.2) and (5.3) is lower than in the other cases, as

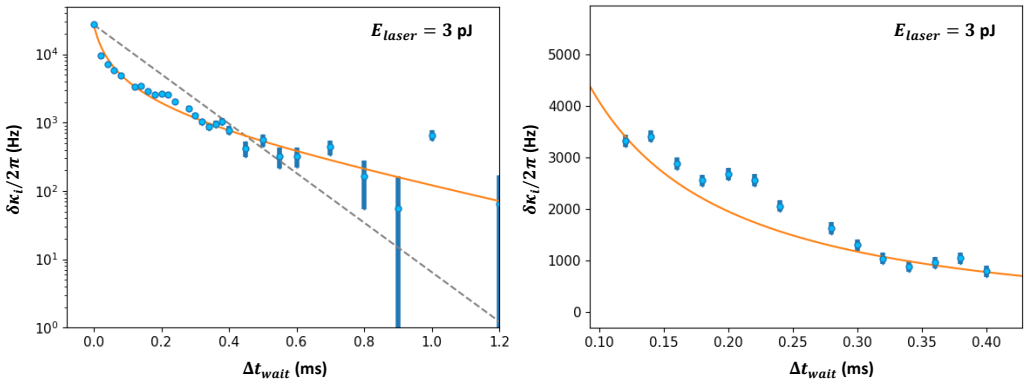


Figure 5.7.: Time evolution of the extracted resonator internal loss rate (**left**) and a zoom on the oscillating behavior(**right**), for a low laser pulse energy of $E_{laser}$ = 3pJ. The data points include also the fitting standard error. In gray is the simple exponential decay fit. In this case $P_{laser} = 6\,\mu$W and $\tau_{laser} = 500$ ns.

shown in Fig. 5.7. It is likely that the fitting model is not accurately representing the physics of the system. Indeed, the laser beam pulse generates a large quasiparticle density $x^i_{qp}$ localized on the resonator circular pad in a $\sim$ 100 ns time window. In this situation, the role of quasiparticle diffusion is probably not negligible, violating the assumptions of the non-diffusive time evolution model. More complex phonon-quasiparticle interaction processes, also not captured by this model, could lead to a different time evolution. New models are required to overcome these limitations. As a possibility, a further theoretical study could develop a new fitting model starting from the 1D diffusion model, presented in section 2.1.1.

## 5.5. Energy response

In the third experiment we studied response of the resonator to a wide range of laser pulse energies at a fixed delay time $\Delta t_{wait}$. The experiment parameters are shown in Table 5.6.

| | |
|---|---|
| $\tau_{laser}$ | $240\,ns$ |
| $\tau_{VNA}$ | $10\,\mu s$ |
| $\Delta t_{wait}$ | $10\,\mu s$ |

Table 5.6.: The fixed experimental parameters for the energy response experiment.

The laser pulse time was kept fixed and the laser energy was swept from 0 to $150\,pJ$

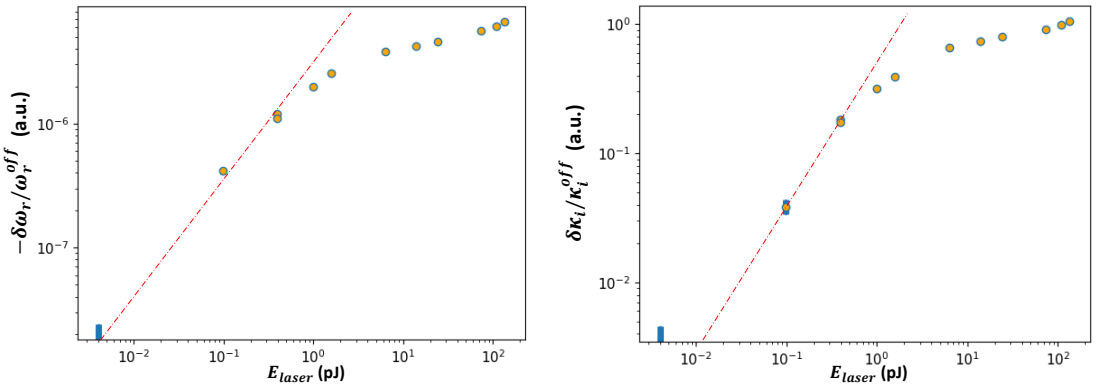


Figure 5.8.: **Left** The change in the resonator internal loss rate with respect to the laser pulse energy normalized to $\omega_r^{off}$ the resonator frequency when the laser is off. **Right** The change in resonance frequency with respect to the laser energy pulse normalized to $\kappa_i^{off}$ the resonator internal loss rate when the laser is off. A red dotted line indicates the linear dependence for low laser power.

and the collected data is shown in Fig.5.8. The response of the resonator is presented through the shift in the loss rate $\delta\kappa_i = \kappa_i^{on} - \kappa_i^{off}$ (with $\kappa_i^{on/off}$ the loss rate when the laser is respectively on or off) and resonance frequency $\delta\omega_r = \omega_r^{on} - \omega_r^{off}$ (with $\omega_r^{on/off}$ respectively the frequency when the laser is on or off).

For $E_{laser} < 1\,\text{pJ}$, $\delta\omega_r$ and $\delta\kappa_i$ follow a linear growth. Supposing to be in the regime $\delta\omega_r \propto -\delta x_{qp}$ and $\delta\kappa_i \propto \delta x_{qp}$, this means that the injected normalized quasiparticle density $x_{qp}^i$ is linearly depending on the laser pulse energy.

For $E_{laser} > 1\,\text{pJ}$, the linear behavior is not anymore verified and we see a slower growth of $\delta\omega_r$ and $\delta\kappa_i$ . This could be due to the fact that for high-enough injected quasiparticle densities $x_{qp}^i$ the linear approximation breaks down $\delta\omega_r \not\propto -\delta x_{qp}$ and $\delta\kappa_i \not\propto \delta x_{qp}$. The slower growth could also be justified by a partial saturation of the injected quasiparticles at the resonator circular pad, where the laser is shining. The breaking of Cooper pairs by infrared photons could start being in a dynamic equilibrium with quasiparticles diffusion across the resonator and relaxation. This hypothesis could be easily tested by checking if a steady value of of $\delta\omega_r$ and $\delta\kappa_i$ is reached at higher energy.

## 5.6. Implications for the transduction experiment

It is possible to use the collected data from the resonator response to draw some useful conclusions for the final microwave to optic transduction experiment (introduced in section 1). From the setup of Fig. 1.1 it is possible to see the qubit interacting with the HBAR inside an optical cavity. Let us give some reference values for the experiment.

Using a high finesse optical cavity, with mirrors reflectivity $R = 99.9\,\%$, it is possible to achieve a mirror coupling loss rate of $\kappa_C/2\pi \approx 2\,\text{MHz}$, this yields a total cavity linewidth

of $\kappa/2\pi = 2\kappa_C/2\pi \approx 4\,\text{MHz}$. Moreover, the HBAR internal loss rate can be assumed to be $\gamma/2\pi \approx 450Hz$ [32]. In a separate work carried out in the Hybrid Quantum Systems Group, Alexandra Bernasconi estimated that for performing a complete phonon-photon optomechanical conversion, we need an intracavity photon number of $n \approx 85 \cdot 10^3$ and a laser pulse length of $\Delta t \approx 11\,\mu\text{s}$. The intracavity photon number gives us a final laser power inside the cavity as $P_{cavity} = \frac{\hbar\omega_{IR} \cdot n\kappa_C}{1-R} \approx 20\mu\text{W}$ and a final pulse energy :

$$E_{cavity} = P_{cavity} \cdot \Delta t \approx 1.5\,\text{nJ}.$$

However, in the final experiment we will not shine the laser beam directly onto the superconducting device. We can assume that then only a $10\% - 0.1\%$ of the total light will get absorbed by the superconductor, with a final absorbed energy $E_{sc} = 150 - 1.5\,\text{pJ}$.

From Fig. 5.8 it is possible to see that laser pulse energies of this order are able to produce a shift in the resonator internal loss rate and frequency of $|\delta\kappa_i|, |\delta\omega_r| \approx 10^4\,\text{Hz}$. The change of the resonator loss rate is of the same order of magnitude as the resonator line-width when the laser is off $\delta\kappa_i/\kappa_i^{off} \approx 1$. Using the data collected for $E_{sc} = 3 - 300\,\text{pJ}$ (section 5.4) and supposing the non-diffusive time evolution model to be reliable it would be possible to obtain a quasiparticle decay characteristic time of $\tau_{ss} \approx 105 - 400\,\mu\text{s}$. However, even if the fitting model proved to be not enough accurate for our system, we see that for $\Delta t_{wait} > 1.2\,\text{ms}$ $\delta\omega_r, \delta\kappa_i \to 0$[i] in this energy range.

It is interesting to notice that, even if at higher pulse energies the change in the resonator linewidth $\delta\kappa_i$ and resonator frequency $\delta\omega_r$ are more dramatic, it is still true that for $\Delta t_{wait} > 1.2\,\text{ms}$ $\delta\omega_r, \delta\kappa_i \to 0$. This constant time dynamic was experimentally observed only for the energy values of Table 5.5, and more data may be needed to confirm it.

For the transduction experiment it would be then safe to use a recovery time

$$\Delta t_{idle} = 1.5\,\text{ms}$$

between subsequent laser pulses. This would finally yield a repetition rate of

$$f_{exp} \sim 600 - 700\,\text{Hz}.$$

These observations are based on the data collected using an electrical resonator. As outlined in section 2.4, it is possible the qubit will exhibit a different response and recovery time. Indeed, the presence of the Josephson junction and the different geometry can determine a different response to quasiparticles and time dynamic.

[i] actually $|\delta\kappa_i| < 90\,\text{Hz}$, which is inside the error bar for the fitting estimations of $\kappa_i$

Part 2

# Qubit design for quantum transduction

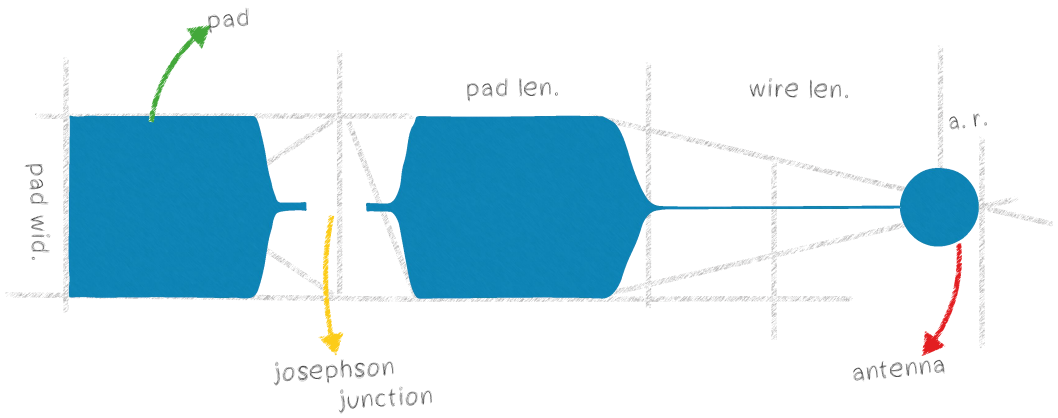


*"Simplicity is the ultimate sophistication."*
*Leonardo Da Vinci*

Chapter 6

# Theoretical background

The process of designing an experiment for quantum microwave to optical transduction requires the ability to design superconducting qubits and a readout architecture for interacting with the qubit itself.

In this chapter we will review the basic theoretical concepts needed for performing high frequency transmon qubit design, qubit readout and control. We will start by introducing the fundamental characteristic of the transmon qubit. We will then move to circuit QED, presenting the 'strong dispersive' regime. We will then finally give a quick outline of the Purcell effect for a qubit interacting with a readout resonator.

This chapter is not at all to be intended as a comprehensive presentation, but more as a quick review of the basic concepts required for going through the next chapters.

## 6.1. The transmon qubit

The transmon is composed by two superconducting islands connected by two Josephson Junctions (SQUID) [i]. The circuit structure (Fig. 6.1 ) is similar to the one of the Cooper pair box [34], but the two superconductors are now also connected through a large shunting capacitance $C_B$.

As in the case of the Cooper pair box the Hamiltonian for this system is [33]:

$$H = 4E_c(\hat{n} - n_g)^2 - E_J \cos\left(\hat{\phi}\right) \tag{6.1}$$

with $\hat{n}$ the number of Cooper pairs tunneling across the islands, $\hat{\phi}$ the gauge-invariant phase between the superconductors, $n_g$ the effective offset charge of islands [34], $E_J$ the Josephson energy and $E_C$ the charging energy.

In the case of a SQUID, with identical Josephson Junctions, the Josephson energy is:

$$E_J = E_J^0 \cos\left(\frac{\Phi}{\Phi_0}\pi\right) \tag{6.2}$$

$$E_J^0 = \frac{\Phi_0 I_c}{2\pi} \tag{6.3}$$

where $\Phi$ is the total magnetic flux across the Josephson junctions circuit loop, $\Phi_0$ the

[i] Only one Josephson junction if we are not interested in flux tunability [33].

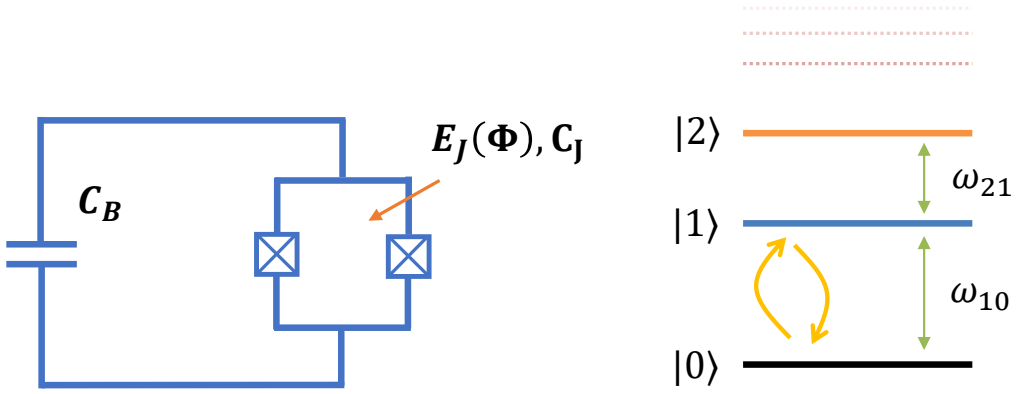


Figure 6.1.: **Left** Circuit of the transmon qubit. $C_b$ is a large capacitance in parallel with the Josephson junctions. **Right** Energy structure the transmon qubit. Thanks to the anharmonic level structure it is possible to selectively control the $|0\rangle \leftrightarrow |1\rangle$ through MW pulses at the frequency $\omega_{10}$.

quantum flux and

$$I_c = j_c \cdot A \tag{6.4}$$

the critical current of the Josephson Junction, depending on the total cross section area of the junctions $A$ and on the critical current density $j_c$.

The charging energy is defined as [33]:

$$E_C = \frac{e^2}{2C_\Sigma} \tag{6.5}$$

$$C_\Sigma = C_B + C_J + C_g \tag{6.6}$$

with $C_g$ the gate capacitance[33] and $C_J$ the total capacitance associated to the Josephson junctions.

By solving equation (6.1) it is possible to see that the system behaves as an anharmonic oscillator, with energy levels schematically shown in Fig. 6.1. In this framework the qubit ground and excited states, $|0\rangle$ and $|1\rangle$, represent the two possible logical states of the qubit.

The system being anharmonic means that the energy distance between adjacent levels changes:

$$\omega_{i,i-1} \neq \omega_{i+1,i}$$

with $\hbar\omega_{ij}$ the energy difference between levels $i$ and $j$. This property allows to use MW pulses to selectively address the $|0\rangle \leftrightarrow |1\rangle$ energy transition, giving us the ability to control an effective quantum two-level system, that could be used as a qubit. As in Ref.

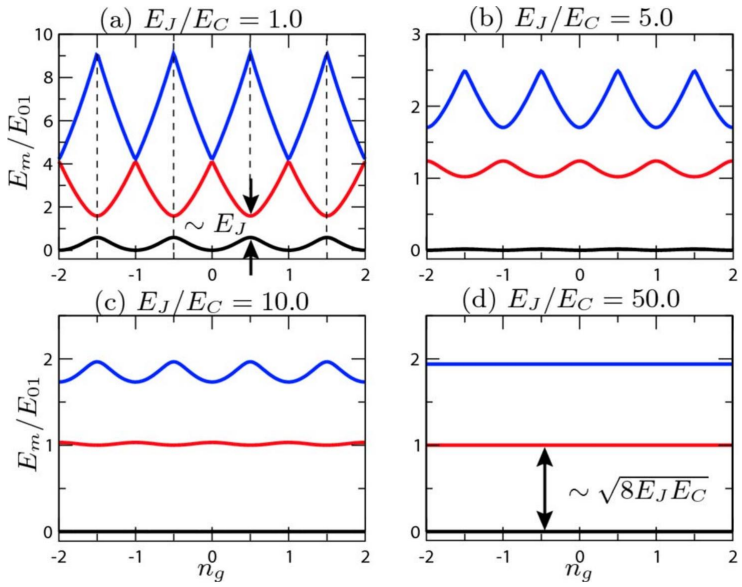


Figure 6.2.: Plot of the lowest energy levels ($E_0$, $E_1$, $E_2$) with respect to the charge offset value $n_g$, with different values of $E_J/E_C$. Picture taken from [33].

[33] the anharmonicity of the system can be defined as:

$$\alpha = \omega_{21} - \omega_{10}$$

and the relative anharmonicity as

$$\alpha' = \alpha/\omega_{10}$$

.

### 6.1.1. Transmon regime

The qubit is said to be in the transmon regime if $E_J/E_C \gg 1$. When this condition is satisfied, the energy levels of the system $E_i$ are relatively insensitive to the change of the offset charge $n_g$ (Fig. 6.2). This condition is one important requirement for achieving longer decay and coherence times $T_1, T_2$ [35, 36].

Let us outline the formulas for the qubit frequency and relative anharmonicity in the transmon regime [33]:

$$\hbar\omega_{10} \approx \sqrt{8E_CE_J}, \tag{6.7}$$

$$\alpha' \approx \sqrt{\frac{E_C}{8E_J}}. \tag{6.8}$$

Formula (6.8) shows that the price to be paid for being in the transmon regime is a

loss in relative anharmonicity $\alpha'$ . Indeed the more the ratio $E_J/E_C$ grows the more the $\alpha'$ decreases.

## 6.2. Interacting with the qubit

The idea behind the control and interaction with a superconducting qubit is based on methods developed in cavity quantum electrodynamics (CQED) [37]. In optical CQED systems atoms couple through dipole interaction with an electromagnetic field mode confined inside an optical cavity. Using a free space laser it is possible to drive the cavity and readout the state of the atom, which acts as a two level system. In superconducting circuits the atom is exchanged with the qubit (artificial atom) and the optical cavity is exchanged with a superconducting resonator (readout resonator) [38]. Instead of using a free-space laser, in circuit QED transmission lines route the input and output signals towards and from the device under test (DUT).

There are many possible realization for the readout resonator, from co-planar strip-line resonators [39] to 3D microwave cavities [36]. Also many different qubit realizations are possible. In our case we will consider the qubit to be a transmon.

The equivalent circuit structure of the outlined system is shown in Fig. 6.3. The Hamiltonian is [40]:

$$H = H_{qr} + H_{drive} \tag{6.9}$$

where

$$H_{qr} = H_0 + \hbar g(\hat{a}\sigma^+ + \hat{a}^\dagger\sigma^-) \tag{6.10}$$

with

$$H_0 = \hbar\omega_r\hat{a}^\dagger\hat{a} + \frac{\hbar\omega_q}{2}\sigma_z, \tag{6.11}$$

$\omega_r$ the resonance frequency of the resonator, $\hat{a}$ the annihilation operator for resonator photons, $\omega_q$ the qubit frequency, $\sigma_z$ the Pauli-Z operator for the qubit, $\sigma^-$ and $\sigma^+$ respectively the lowering and rising operator for the qubit state and $g$ is the coupling rate between the resonator and the qubit.
Here $H_{drive}$ represents the resonator and qubit driving term.

### 6.2.1. The strong dispersive regime

In the dispersive regime the following condition holds:

$$|\Delta| = |\omega_r - \omega_q| \gg g$$

which means the qubit is far detuned in frequency from the cavity. In this case, starting from equation 6.10 and applying the Schrieffer–Wolff transformation yields the final

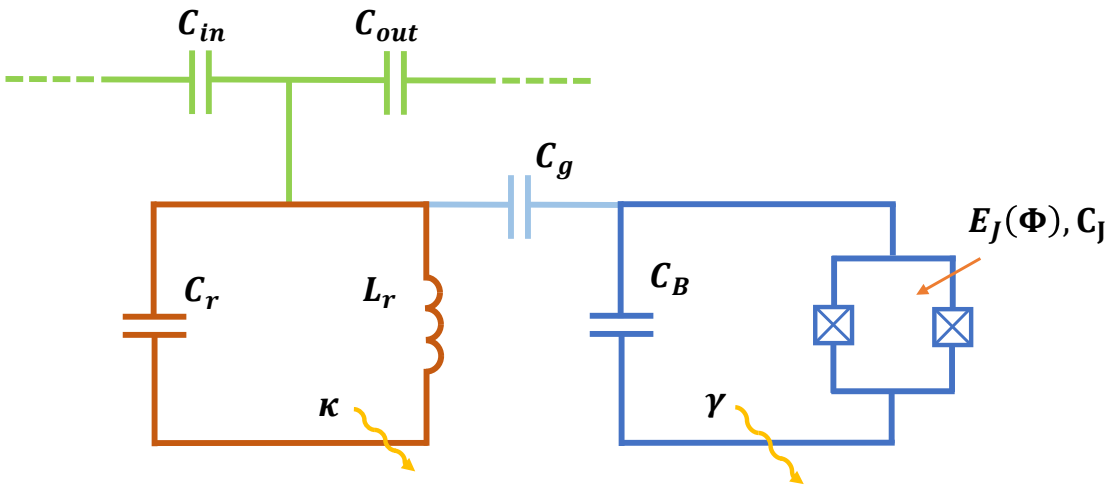


Figure 6.3.: Circuit representation of the complete basic circuit QED architecture. The input-output transmission line (green) couples capacitively through $C_{in}$ and $C_{out}$ with the readout resonator (orange), which is represented as a lumped LC inductor with $L_r$ and $C_r$. The resonator couples to the qubit (in blue) through an effective capacitively coupling $C_g$ (in light blue). Both the resonator and the qubit have an associated energy decay rate into the environment $\kappa$ and $\gamma$.

approximated Hamiltonian [40]:

$$H_{dis} \approx H_0 + \hbar\chi \left(\hat{a}^\dagger \hat{a} + \frac{1}{2}\right) \sigma_z \tag{6.12}$$

with

$$\chi = \frac{g^2}{\Delta} \tag{6.13}$$

being the dispersive shift.

From eq. 6.12 we see that, to a first order approximation in $\frac{g^2}{\Delta}$, the resonator and the qubit are not directly exchanging excitations. However, the qubit will induce a shift $\chi$ in the resonator frequency

$$\omega_r' = \omega_r \pm \chi$$

according to its excited or ground state. The qubit-induced change in the resonance frequency of the resonator will lead to a change in the amplitude or phase of the photons transmitted by the resonator and it is the basis for performing quantum non-demolition (QND) readout of the qubit [40].

Being in the dispersive regime is however not enough. In order to have a coherent interaction between the qubit and the readout resonator we need to enter the strong

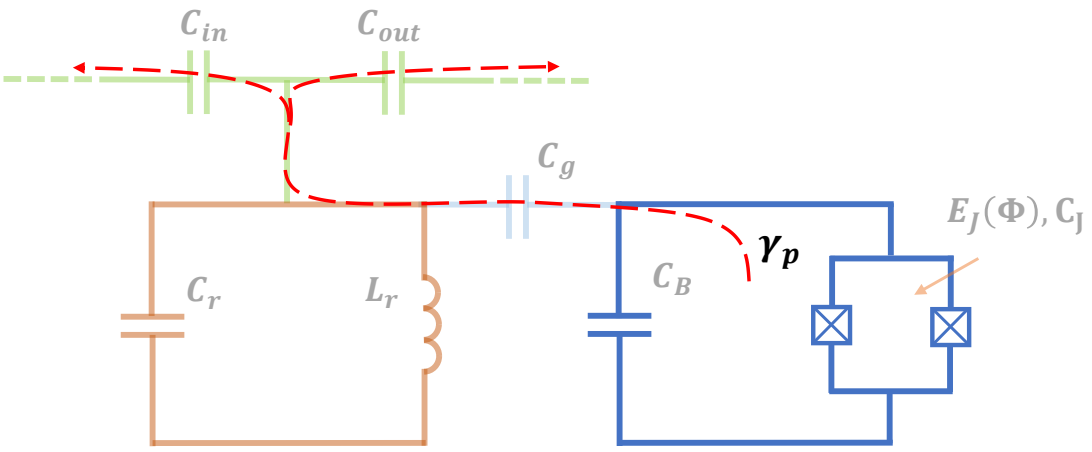


Figure 6.4.: The Purcell effect induces decay of the qubit into the readout transmission line through the readout readout resonator.

dispersive regime [40, 41], fulfilling the additional condition:

$$g \gg \gamma, \kappa$$

with $\gamma$ and $\kappa$ respectively the qubit and resonator decay rate.

### 6.2.2. Purcell effect

The Purcell effect is the modification of the spontaneous decay rate of a qubit, interacting with a resonator, into the transmission line (Fig. 6.4). It has been shown that, in the case of strong dispersive regime, the interesting regime for us, the Purcell decay could be approximated to be [33, 40]:

$$\gamma_p \approx \frac{g^2}{\Delta^2}\kappa \tag{6.14}$$

It is worth noticing that equation 6.14 is a good approximation only if $\Delta \gg \kappa$, which is always true in our designs. Moreover, in the case of strong dispersive regime $g/\Delta \ll 1$ leads to a suppression of the Purcell decay with respect to cavity linewidth $\gamma_p \ll \kappa$.

Chapter 7

# High frequency qubit design

A goal of the project was to design and simulate a high frequency transmon. Indeed, in order for a qubit to be able to interact with the HBAR device and start the transduction process, the qubit fundamental frequency $\omega_q$ needs to be equal to the Brilluoin frequency of the material used for designing the HBAR. At this point of the project it is still not known which is the final material that is going to be used but there is a list of candidates. This put a boundary on the final wanted qubit frequency to be between 8.5 GHz $< \omega_q^{new}/2\pi <$ 13.4 GHz, with 8.5 GHz being the Brilluoin frequency of $BaF_2$ and 13.4 GHz being the one of $CaF_2$.

As introduced in the theory chapter two of the important quantities of interests in qubit design are $E_J$ the Josephson energy and $E_C$ the charging energy. When designing a high frequency qubit transmon it is important that the design achieves the wanted target frequency $\omega_q^{new}$ and respects the requirements to be a transmon (section 6.1.1). The strategy followed is shown in Fig.7.1. We started from an old working qubit design from the group and we extract the values $\omega_q^{old}$, $E_J^{old}$ and $E_C^{old}$. We then find the new values of $E_J^{new}$ and $E_C^{new}$ needed to achieve $\omega_q^{new}$ such as that

$$E_J^{new}/E_C^{new} \approx E_J^{old}/E_C^{old}. \tag{7.1}$$

This will guarantee us to have a higher frequency qubit still in the correct working transmon regime. Let us give a more detailed step of the process.

## 7.1. Old qubit simulation

The first step requires to extract the properties of an old working qubit. We import the .gds file describing the qubit design into Ansys, a 3D electromagnetic simulation software, and we perform an eigenmode simulation. We define the qubit geometry as a perfectly conducting surface. Moreover we define lumped inductors in place of the Josephson junctions as shown in Fig. 7.2 . The value of the lumped inductance is defined by the design properties of the Josephson Junction (among those the junction area). By performing these operations the qubit pads' geometry will induce a capacitance $C_q$ and the lumped inductors will contribute to an inductance $L_j$ [i].

[i] It is worth noticing that we could add also the capacitance of the Josephson junction. However the contribution of this is only few $\sim fF$ and it is not very significant.

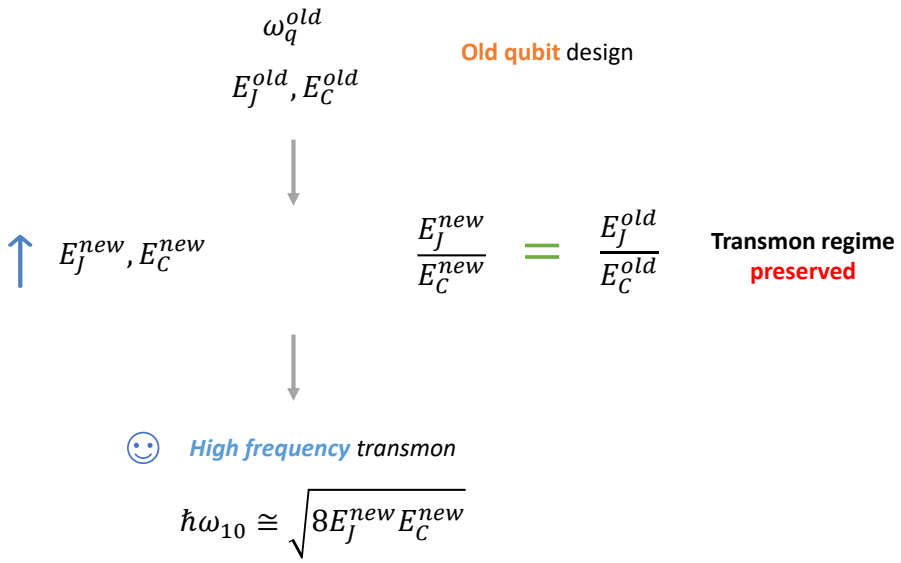


Figure 7.1.: Design strategy for obtaining a new higher frequency transmon starting from an old working design. We increase the value $E_J^{new}$ and $E_C^{new}$ but we leave its ratio constant to be in the same transmon working regime.

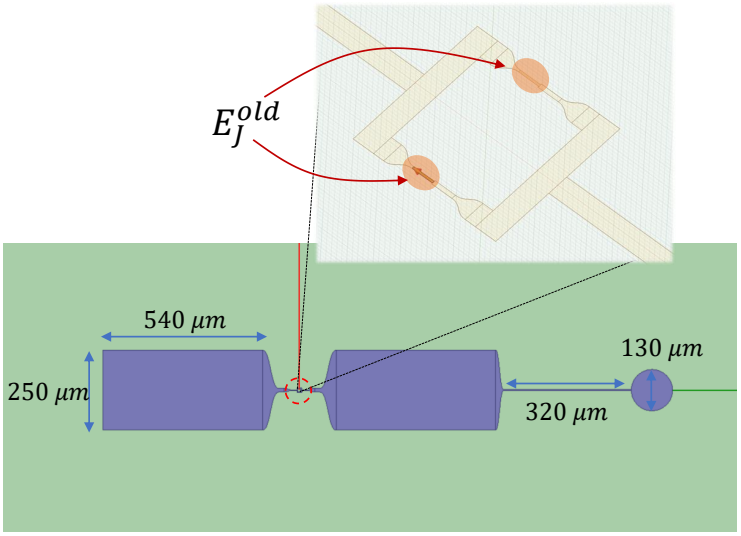


Figure 7.2.: Old qubit gds file, already imported in Ansys. It is possible to read the different characteristic dimensions defining the design. The inset shows the detail of two Josephson junctions (the qubit is a SQUID) which are modeled by defining an lumped inductor on Ansys with inductance value $L_J^{old}$ linked to $E_J^{Old}$.

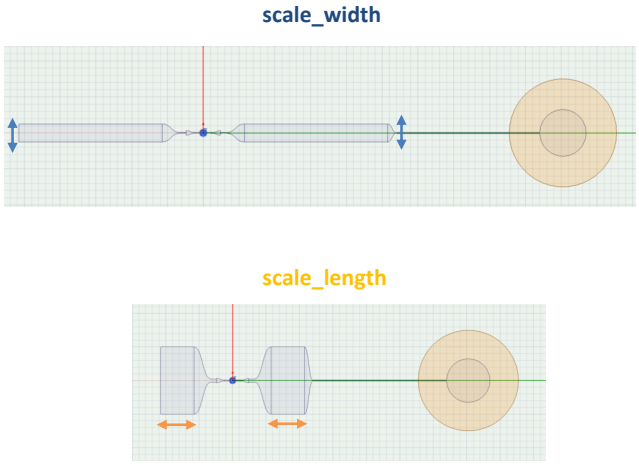


Figure 7.3.: Examples of qubit geometry parametrization. **Top** Changing the width of the pads by using the parameter *scale_ width*. **Bottom** Changing the length of the pads by using the parameter *scale_ length*.

In Ansys we reduce the qubit to a simple LC oscillator and so to an harmonic system. This however is not problematic as we aim at simulating only the fundamental qubit frequency, which is represented by the first mode of the harmonic oscillator qubit version. We perform an eigenmode simulation and we obtain the qubit frequency $\omega_q^{old}$ that, combined with our knowledge of $E_J^{old}$[ii], gives us a defined value of $E_C^{old} = (\hbar\omega_q^{old})^2/8E_J^{old}$.

## 7.2. New qubit simulations

After obtaining the values $\omega_q^{old}$, $E_J^{old}$ and $E_C^{old}$, we can define the new values $E_J^{new}$ and $E_C^{new}$. $E_J^{new}$ will determine a modification of the Josephson Junction area (equation (6.4)). $E_C^{new}$will determine a new qubit pads geometry. For finding it we perform an Ansys Optimetrics eigenmode analysis of the qubit. We first set the new value of $E_j^{new}$ to our design, through the lumped inductance value. We then define the qubit geometry to be parametric and we sweep the different parameters (Fig. 7.3) each time simulating the frequency of the qubit $\omega_q^i$ with $i$ indicating the index of the simulation. We then collect all this data and we use a Mathematica script to determine all possible candidates that gave us a frequency which is approximately the target one $\{\omega_q^i | \omega_q^i \approx \omega_q^{new}\}$ . This property will guarantee also that the ratio presented in eq. (7.1) is respected.

[ii]The value of $E_J^{old}$ was computed from a reference value for the Josephson Junction inductance of $L_J = 7\,\text{nH}$.

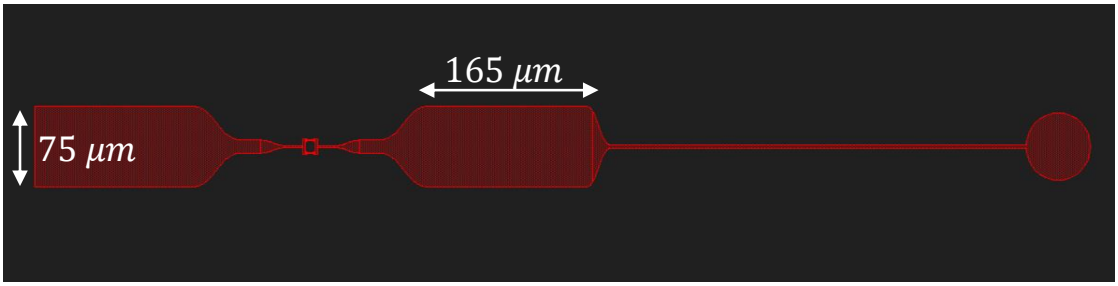


Figure 7.4.: Final qubit design with a frequency $\omega_q^{new}/2\pi = 13.84$ GHz realized as a proof of concept.

## 7.3. Finalizing new design

After determining the desired qubit dimensions it is then possible to use a gdsPy Python script to generate the final qubit gds files. This design is then simulated one last time to check if the frequency is in range.

As a proof of concept we designed a new qubit with a target frequency of $\omega_q^{tg} = 13.6$ GHz, starting from an initial old design qubit $\omega_q^{old}/2\pi = 5.71$ GHz. We were able to obtain a qubit with a final frequency of $\omega_q^{new}/2\pi = 13.84$ GHz and $E_J/E_C \sim 130$ hitting the transmon regime. The final design is shown in Fig. 7.4.

Chapter 8

# Optical Cavity Integration

In the previous chapter we described the design of a transmon qubit with $\omega_q$ matching the Brillouin frequency of the HBAR. A second step toward optomechanical transduction was to create a platform to interact with the qubit and read out its state. The basic elements needed to interact with the qubit consist of a readout line and a readout resonator. We point out that, in our design, the readout resonator needs to have a frequency $\omega_r \approx 10\,\text{GHz}$, $\sim$ GHz distant from the final qubit frequency (as outlined in chapter 7).

Another requirement for the qubit platform is to be compatible with the optical cavity. Fig. 8.1 shows that the readout architecture should fit between the flat and the convex mirrors of the optical cavity. This is quite challenging, as the maximum distance between the mirrors can be $\sim 11 - 12\,\text{mm}$. The tight space requirements make the usual 3D readout cavity designs very hard to implement. Indeed, overcoming the fitting challenge required a complete shift of perspective. The Axline geometry [27] is a hybrid architecture combining an on chip resonator and qubit with a 3D tunnel cavity for suppressing decay into the environment.

In this chapter we first describe the Axline geometry, we then introduce a first working proof of concept (simulated in Ansys HFSS) and finally we present a first study of the influence of the laser hole on the simulated qubit decay rate $\gamma_{sim}$ .

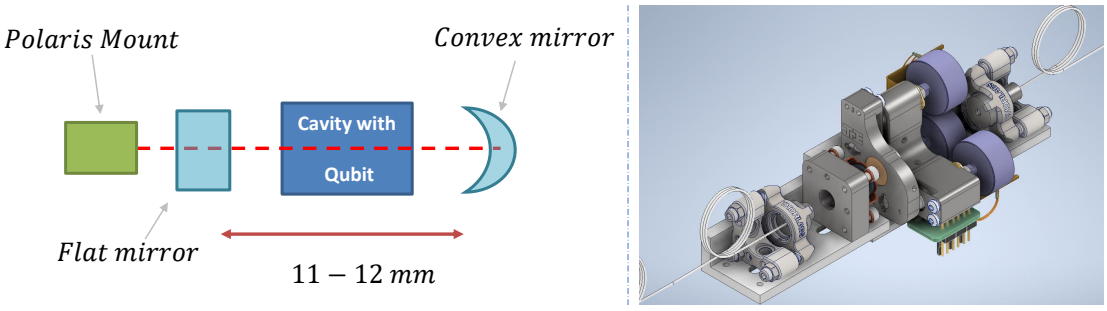


Figure 8.1.: **Left** Sketch showing how the qubit platform should be integrated in the optical cavity. **Right** 3D CAD model of the optical cavity.

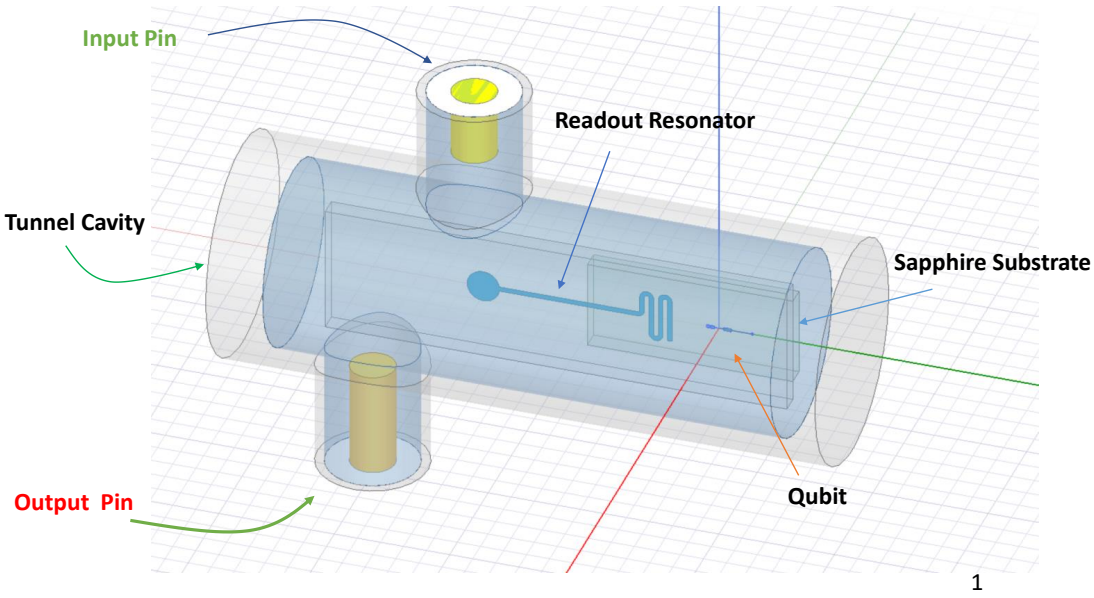


Figure 8.2.: Outline of the structure composing the Axline platform.

## 8.1. Axline geometry

The Axline geometry is inspired by qubit readout platform designed in Ref. [27] and it is shown in Fig. 8.2. Let us analyze the main element composing this structure.

### 8.1.1. Tunnel cavity

The tunnel cavity suppresses the decay of the qubit and the readout resonator into the environment. This structure can be manufactured out of a single piece of aluminum, guaranteeing no seam losses [27]. Moreover at mK, aluminum becomes superconductive ($T_c = 1.2$ K), and the cavity walls do not dissipate energy from the confined EM field of the qubit or readout resonator. This guarantees higher quality factors both for the read out resonator $Q_r$ and the qubit itself $Q_q$. The final important design dimensions of the tunnel cavity are shown in table 8.1, with $d$ and $D$ respectively the internal and external tunnel diameters and $l$ the tunnel length.

| $d$ | $D$ | $l$ |
|---|---|---|
| 4 mm | 6 mm | 13 m |

Table 8.1.: Parameters defining the final Axline tunnel structure that will be implemented in the optical cavity integration project.

The dimensions of this device are very favorable for an integration with the Optical

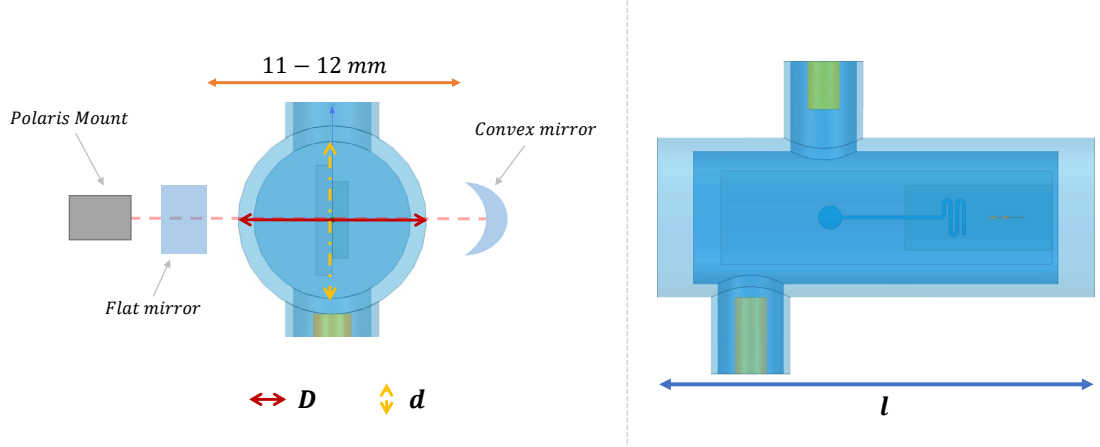


Figure 8.3.: **Left** The tunnel cavity inside the schematically drawn optical cavity. The quantities $D$ and $d$ are shown. **Right** A different view of the tunnel cavity showing the parameter $l$

cavity. As shown in Fig. 8.3 with an external diameter of $D = 6\,\text{mm}$ it is possible to easily fit the device between the two mirrors of the optical cavity.

A simple eigenmode simulation was performed showing a fundamental cavity mode of 30 GHz. This guarantees also that the qubit ( 13.6 GHz) and readout frequency modes ( 10 GHz) to be distanced in frequency with respect to the fundamental cavity modes.

### 8.1.2. Qubit and readout resonator

The readout resonator and the qubit are both placed on a single sapphire chip (Fig. 8.4).

The readout resonator is characterized by a hybrid architecture. It has a circular pad, to increase the capacitive coupling between the resonator and the input-output pins. It then continues with a straight strip-line geometry and ends with a meandering structure that increases the coupling between the qubit and the resonator itself.

The qubit used for these simulations is a high frequency design briefly presented in sec. 7.3, with a simulated frequency $\omega_q/2\pi = 13.84$ GHz.

### 8.1.3. Input-output pins

The readout of the qubit is performed in transmission. This means that we need an input and output line interacting with the readout resonator. In our case this is realized by input-output pins, capacitively coupling with the resonator. To achieve a high readout efficiency the information contained into the resonator needs to leak almost completely into the output line. This requires the coupling of the resonator with the input line $\kappa_{in}$ to be much smaller than the coupling with the output one $\kappa_{out}$:

$$\kappa_{in} \ll \kappa_{out}.$$

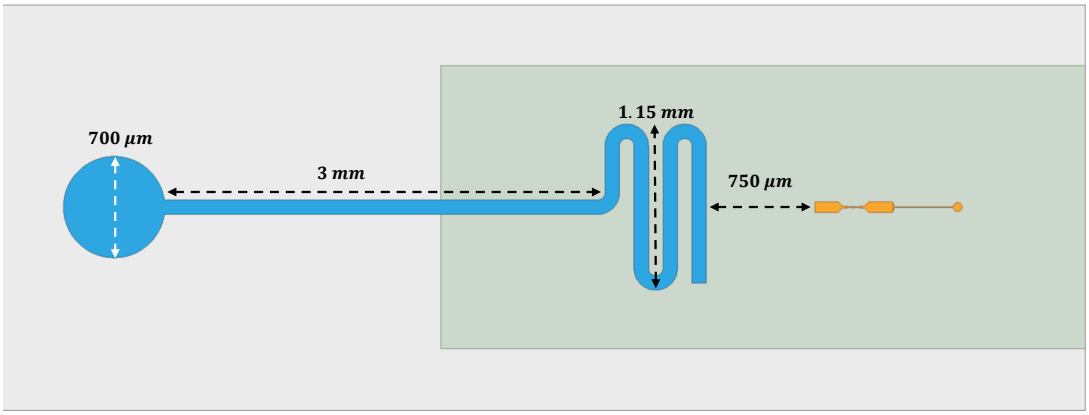


Figure 8.4.: Figure showing the qubit and the readout resonator, with some characteristic dimensions indicated.

As a rule of thumb we decided $\kappa_{out} \approx 10\,\kappa_{in}$.

The coupling of each single pin with the resonator can easily be scaled by changing the insertion length of it. As shown in Fig. 8.5 the coupling to the output pin with respect to its distance from the edge of the tunnel cavity $h_{pin}^{out}$ shows an exponential dependence.

It is important to notice that not only the resonator couples capacitively to the input-output pins but also the qubit can do this. By defining the coupling rate of the qubit to the pins $\gamma_{qp}$ and the total decay rate of the qubit $\gamma$ it is important that

$$\gamma_{qp} \ll \gamma.$$

In general this condition is easily fulfilled. However, the small dimensions of the design implemented in this project can lead to a dangerous increase of $\gamma_{qp}$, drastically influencing the qubit lifetime. Indeed, the input pin is nearer to the resonator then the output pin to decrease $\gamma_{qp}$ as much as possible (Fig. 8.2).

The complete circuit representation of the qubit, readout resonator and readout line is presented in Fig. 8.6.

The pin diameter is $d_{pin} = 1$ mm, a value respecting the dimensions used for the pins for other designs.

### 8.1.4. Simulation of $\kappa$ and $\gamma$

In order to simulate $\kappa_{out}$, $\kappa_{in}$ and $\gamma_{qp}$ we perform an Ansys eigenmode simulation. We define the pin material to be of perfect conductor and we define one of the ending surfaces to have a lumped R value of $50\,\Omega$. The Ansys simulation will provide us the mode frequency of the readout resonator $f_r$ and of the qubit $f_q$ and the associated quality

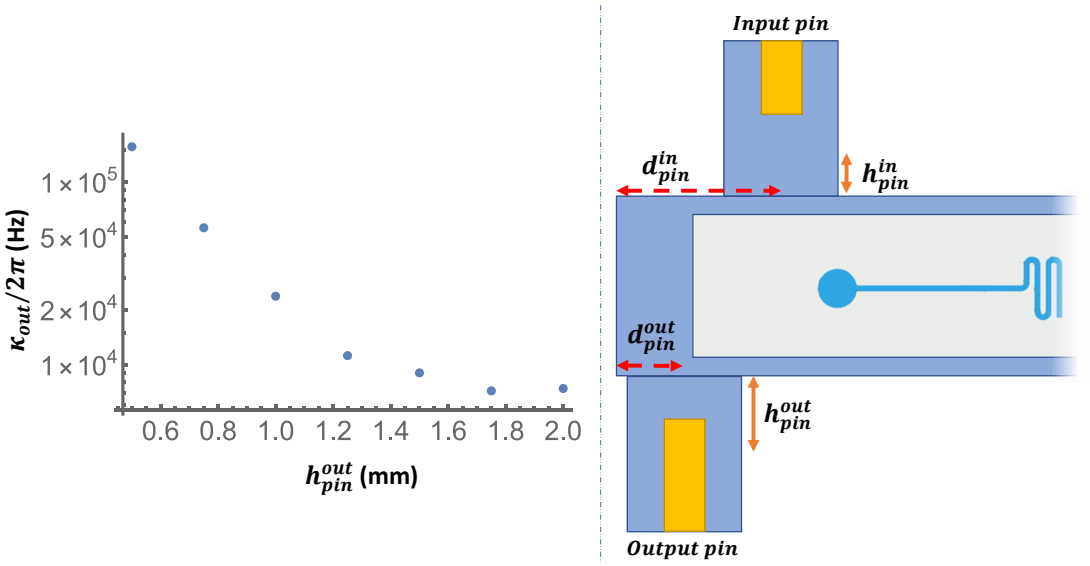


Figure 8.5.: **Left** The output coupling $\kappa_{out}$ with respect to distance from the end of the output pin to the edge of the tunnel enclosure $h_{pin}^{out}$. **Right** Graphical representation of the tunnel with the input and output pins. $d_{pin}^{out}$ and $d_{pin}^{in}$ are the distance of the pins (from their center) to the left end of the tunnel.

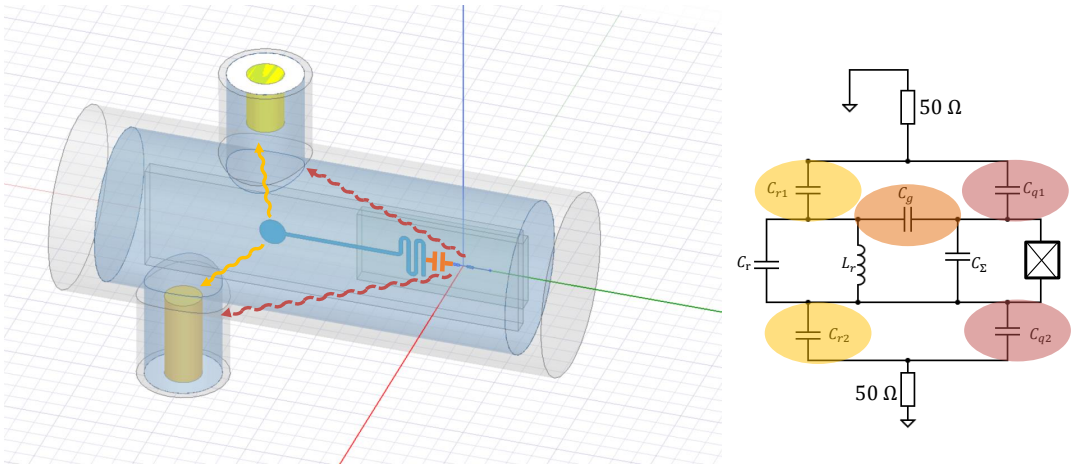


Figure 8.6.: Circuit schematic. The transmission lines are modeled using a 50 Ω impedance. The pin coupling between the resonator and the input-output pins is represented by $C_{r1}$ and $C_{r2}$, while the coupling between the pins and the qubit is represented by $C_{q1}$ and $C_{q2}$. The coupling between the resonator and the qubit is represented by $C_g$.

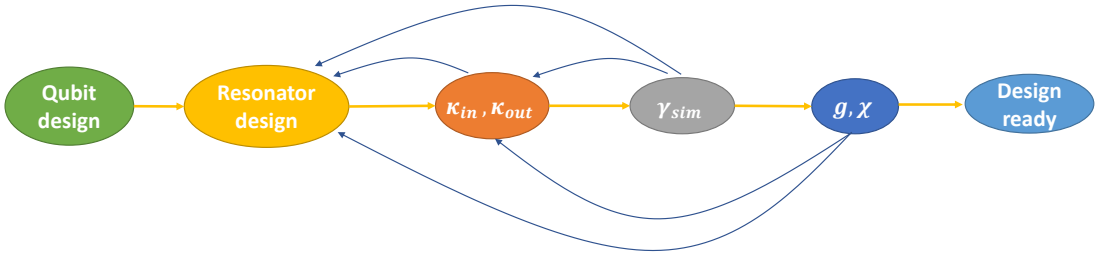


Figure 8.7.: Main design steps.

factor $Q_r$ and $Q_q$. It is then possible to extract the loss rates by using the formulas

$$\kappa/2\pi = \frac{f_r}{Q_r},$$

$$\gamma/2\pi = \frac{f_q}{Q_q}.$$

For simulating separately $\kappa_{in}$ we temporally disabled the output pin from the design and for $\kappa_{out}$ we did the converse.

## 8.2. Simulation of the Axline structure

The real design process is actually very complex, with many different iterations at different levels. In Fig. 8.7 it is possible to see an outline of the process steps followed. We first perform the qubit design following the qubit pipeline presented in chapter 7. We design a readout resonator, with the wanted frequency $\omega_r$ and with a promising architecture for achieving a good coupling with the input-output pins and the qubit. We then simulate the coupling rate with the readout lines $\kappa_{in}$ , $\kappa_{out}$ and later $\gamma_{sim}$, the simulated qubit decay rate [i]. As a last step we use Py-EPR to extract the coupling between the resonator and the qubit $g$ and the dispersive shift $\chi$. These steps are highly interdependent and the process needs multiple iterations before reaching final promising design . A first working concept version was obtained featuring the parameters shown in table 8.2. In the following sections we will analyze these results.

### 8.2.1. Resonator coupling rate $\kappa_c$

For performing an optimal readout it is beneficial for the resonator to be over-coupled to the output line, such as that most of the information leaks trough the output pin instead of decaying trough other loss channels. This implies $\kappa_{out} \gg \kappa_{int}$, with $\kappa_{int}$ the internal loss rate of a resonator. From previous works [27, 31], it was possible to see that for stripline resonators on sapphire $\kappa_{int} \approx 30 - 70$ kHz. In our design $\kappa_c = \kappa_{in} + \kappa_{out} \sim 70$ kHz

[i] As explained later, Ansys is not able to simulate the main qubit decay sources, limiting the actual qubit lifetime. It is then important that $\gamma_{sim} \ll \gamma$, with $\gamma$ the qubit actual decay rate.

| $f_q$ | $f_r$ | $\gamma_{sim}$ | $\kappa_c/2\pi$ | $\kappa_{out}/2\pi$ | $\kappa_{in}/2\pi$ |
|---|---|---|---|---|---|
| 13.84 GHz | 10.3 GHz | 452 Hz | 75.1 kHz | 71.7 kHz | 7.07 kHz |
| | | | | | |
| $h_{pin}^{in}$ | $h_{pin}^{out}$ | $d_{pin}^{in}$ | $d_{pin}^{out}$ | $\alpha$ | $\chi$ |
| 1.35 mm | 0.25 mm | 2.75 mm | 3.92 mm | 410 MHz | 3.12 MHz |

Table 8.2.: The important parameters obtained in the first working version of our design. $d_{pin}^{out}$ and $d_{pin}^{in}$ are defined in Fig. 8.5.

with $\kappa_{out} \approx 10\kappa_{in}$. Even if the resonator is only critically coupled to the input-output line ($\kappa_c \sim \kappa_{int}$) it is straightforward to increase the coupling to the output pin as shown in Fig. 8.5.

### 8.2.2. Qubit decay rate $\gamma_{sim}$

From the Ansys simulations it is possible to obtain $Q_q$ and from this the qubit mode decay rate $\gamma_{sim}$. It is important to notice that the simulation considers only qubit decay through direct coupling with the input-output pins $\gamma_{qp}$ and through the resonator (Purcell effect) $\gamma_p$. Decay of the qubit due to defect two-level systems, often the limiting factor for qubit lifetime, are not accounted for. We then require:

$$\gamma_p + \gamma_{qp} = \gamma_{sim} \ll \gamma$$

with $\gamma$ the typically measured qubit decay rate. This conditions guarantees that the Purcell decay and the qubit-pin coupling decay are not the limiting factor for qubit lifetime $T_1$. In the case $T_1 = 30\,\mu s$, a usual value for these systems [27] and thus $\gamma/2\pi = 5$ kHz. In our simulations we were able to achieve a $\gamma_{sim}/2\pi = 450$ Hz which fulfill the condition $\gamma_{sim} \ll \gamma$.

### 8.2.3. Qubit resonator interaction

The design of a proper interaction between the qubit and the resonator is one of the central and most delicate point of our simulations. For achieving an efficient read-out it is important that the qubit and resonator are in the strong coupling regime

$$g > \gamma, \kappa_c$$

with $g$ the coupling rate between the resonator and the qubit, and in the dispersive regime

$$\Delta = |\omega_r - \omega_q| \gg g.$$

Moreover, once in the dispersive regime, it is important also that the dispersive shift is much bigger than the total decay rate of the resonator:

$$\chi \gg \kappa_{int} + \kappa_c.$$

This condition guarantees there will be a good contrast between the excited and the ground state when the readout is performed through the resonator.

By using PyEPR [42] it was possible to extract the dispersive coupling

$$\chi/2\pi = 3.12\,\text{MHz}$$

and the qubit anharmonicity:

$$\alpha/2\pi = 410\,\text{MHz}$$

through which we computed the coupling rate:

$$g^2 = \frac{\Delta(\Delta+\alpha)}{2\alpha}\chi$$
$$g/2\pi = 105\,\text{MHz}$$

from which it is possible to see that all the previously outlined conditions are satisfied in our design project.

## 8.3. Laser hole effect

In this section we investigate the effect of adding laser holes to our design. Laser holes are necessary for letting the laser beam shine onto the HBAR chip, inside the tunnel cavity. We first remove the input-output pins and we add two holes with the diameter $d_{hole} = 1\,\text{mm}$ centered on the qubit antenna position. To simulate the effect of free space radiation we then define a lumped resistance on the outer surface of the hole to be $R = 377\,\Omega$, the value of vacuum impedance. To increase the efficiency of the optomechanical conversion the laser beam shape should match the shape of the HBAR mechanical mode we want to interact with. In this regard, it would be beneficial for the flat mirror to sit as near as possible to the HBAR. We studied then the effect of reducing as much as possible the thickness of the tunnel walls and of moving the chip to the edge of the tunnel cavity, towards a laser hole.

We first investigated the dependency of the qubit decay through the laser holes $\gamma_{laser}$ with respect to the tunnel wall thickness $w$. From Fig. 8.8 it is possible to see that, for $w > 0.75\,\text{mm}$, the qubit decay rate is $\gamma_{hole} \ll \gamma$, with $\gamma$ defined as in section 8.2.2. We also observe strong fluctuations of $\gamma_{hole}$ for $w > 1\,\text{mm}$. This is due to the limited simulation precision[ii] and it does not represent a problem as long as the simulation shows that $\gamma_{hole} \ll \gamma$.

A second simulation was performed with a constant wall thickness of $w = 1\,\text{mm}$ and with a variable chip vertical distance from the center of the tunnel $t$. In this case the result is shown in Fig. 8.9. It is possible to see that, only small movement of the qubit are possible. Indeed, for $t > 1\,\text{mm}$ the condition $\gamma_{hole} \ll \gamma$ is not anymore true. This means that if $t > 1\,\text{mm}$ the decay of the qubit mode through the laser hole becomes a primary decay channel, limiting the qubit lifetime $T_1$.

[ii] for $\gamma < 500\,\text{Hz}$ Ansys simulations do not converge.

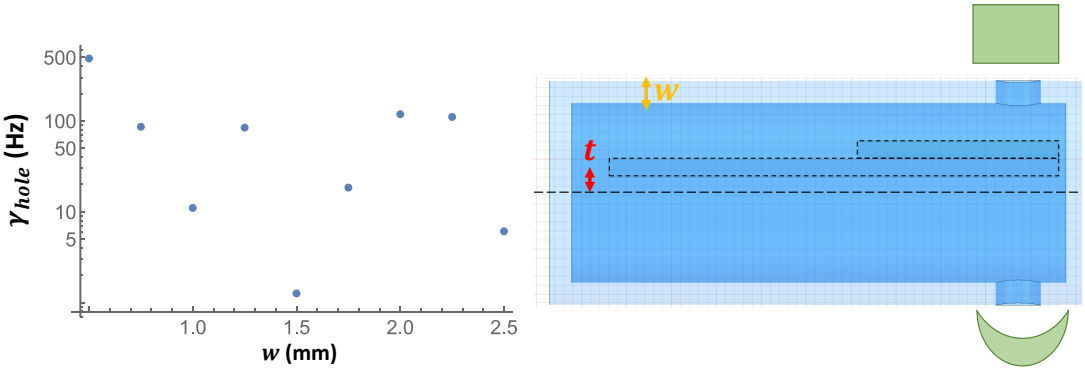


Figure 8.8.: **Left** $\gamma_{hole}$ trend with respect to the wall thickness $w$. For $w > 1\,\text{mm}$ the values of $\gamma_{hole}$ strongly fluctuates due to the simulation imprecision noise. **Right** View of the cavity with the qubit and resonator. $t$ and $w$ are shown for clarity.

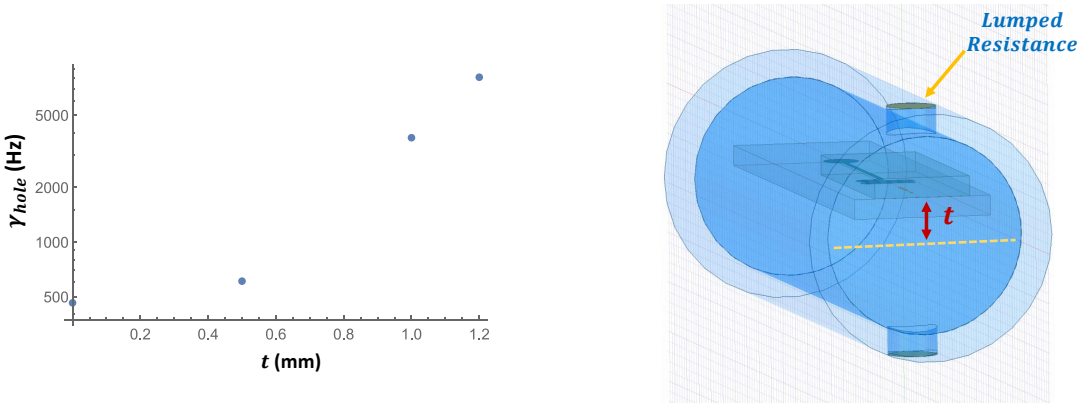


Figure 8.9.: **Left** $\gamma_{hole}$ dependence with respect to $t$. **Right** Representation of the simulated Axline geometry with the laser holes. It is possible to see the 2D surfaces defined at the outer edge of the tunnel, in correspondence of the laser holes, simulating free radiation in vacuum.

# Wrapping up

*"The important thing is never stop questioning."*
*A. Einstein*

*"The future interests me: I'm going to spend the rest of my life there."*
*Mark Twain*

Chapter 9

# Conclusion and outlook

During the course of this Master thesis we pursed two different research projects in the context of quantum microwave to optical transduction.

The first part of this thesis focused on the interaction between infrared (IR) photons and superconducting devices. In chapter 2 we introduced the theory background needed to understand the main experimental results. First we presented two different models describing quasiparticles dynamics, outlining their advantages and limits. We introduced the electrical resonator as a practical tool for investigating the effect of IR laser light on superconductors and we then outlined the poisoning effects of IR-generated quasiparticles on transmon qubits. In chapter 3 we presented the experimental setup. We described the laser control, the microwave electronic and the 3D CAD custom components designed by us and manufactured in collaboration with the DPhys workshop. We then studied the behavior of the fiber collimator and estimated the laser beam misalignment at cryogenic temperatures (chapter 4). We discovered that, in this temperature regime, the former exhibits a final light collection efficiency of $\eta \approx 0.51$. We successfully extracted an average laser beam shift which was confirmed by multiple measurements. In chapter 5, we described the resonator experiment. We presented the main measurement sequence and the fitting techniques adopted. First we performed a power-response experiment. We then investigated the time dynamics of the resonator response to IR light pulses and we tried to adopt a phenomenological fitting model for explaining the time dependence of $\kappa_i(t)$ and $\omega_r(t)$. Unfortunately, the model itself is incomplete and not suitable for our analysis. One of the reasons for this could be the non-negligible role of quasiparticle diffusion in our case. We also discussed how the current measurements allowed us to estimate the repetition rate for the transduction experiment to be 600 - 700 Hz. This value however should be confirmed through study on the qubit IR response. The next step of this project will be investigating the poisoning effect of IR-generated quasiparticles on qubits. As outlined in chapter 2, quasiparticles will directly affect the decay $T_1$ and decoherence time $T_2$ of the transmon. For the electrical resonator study, understanding the time dynamics of $\kappa_i(t)$ and $\omega_r(t)$ requires a more complex quasiparticle model. It would also be interesting to estimate the density of generated quasiparticles $\delta n_{qp}$ from the change in the resonator internal loss rate $\delta\kappa_i$ and frequency $\delta\omega_r$.

The second part of the master project was devoted to qubit design for optomechanical transduction. After presenting a short review of the transmon qubit and introducing the essential tools of Circuit QED (chapter 6), we introduced a pipeline for designing high frequency transmon qubits (chapter 7). Starting from an old transmon qubit design, we described how it is possible to obtain a higher frequency qubit that is still in the cor-

rect working transmon regime. We also proposed a qubit readout and control platform (chapter 8) compatible with high frequency qubits and easy to integrate with an optical cavity. We carried out simulations in Ansys which confirmed that this design could be a promising candidate for the final optomechanical transduction experiment. Manufacturing the tunnel cavity, realizing the qubit and resonator chip in cleanroom, and testing the device inside a dilution refrigerator represent the future phases of this project. If these steps are completed successfully, it will then be possible to integrate this structure inside the optical cavity.

# Appendix

Appendix A

# Experimental setup

## A.1. GRIN Lens

The study of IR light interaction with a superconducting device requires a very precise control of the laser beam position and diameter at focus. Gradient-index (GRIN) lenses are characterised by a refractive index $n(r)$ changing along their radial direction w.r.t to the lens axis. A Gaussian beam, coming from a single mode fiber, exits the GRIN lens with a Gaussian profile at an adjustable waist $w_s$ and working (focus) distance $z_w$ (Fig. A.1). The parameters $w_s$ and $z_w$ depend on the GRIN lens central refractive index $n_g$, length $l_g$, gradient constant $g$ [43], distance between the fiber and the lens $l_0$ and initial beam waist $w_0$.

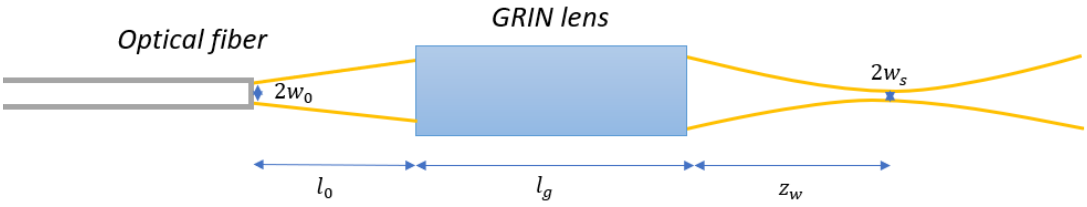


Figure A.1.: GRIN lens assembly graphical representation.

During the course of the project it was possible to design a GRIN lens with a working distance of $z_w = 16.03 \pm 0.1\,mm$ and a beam focus waist $w_s = 51.6 \pm 0.7\,\mu m$ respecting the tight project requirements. Both fiber ferrule and GRIN lens were glued inside a glass sleeve with UV-cured optical glue (type). This sleeve was glued inside a cylindrical steel holder using Stycast glue (type), which was then mounted as shown in Fig. A.2 on a cryogenic-compatible and stable tip-tilt mount with matched coefficients of thermal expansion.

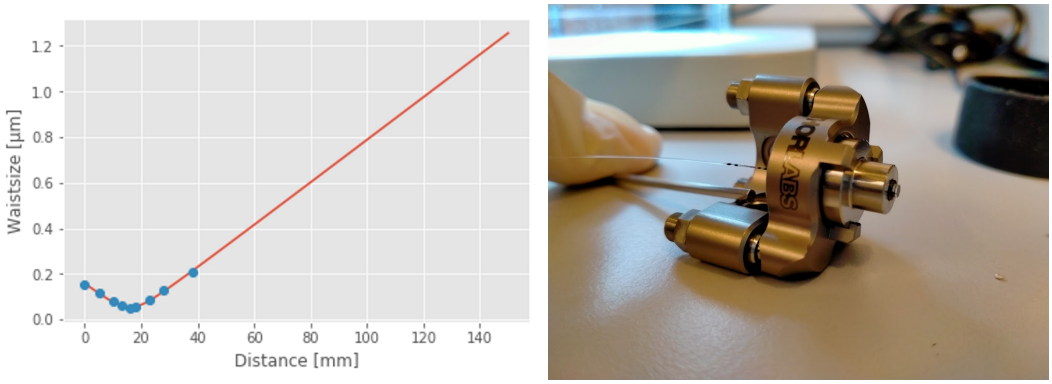


Figure A.2.: **Left** Experimental measurement of the beam waist w.r.t. distance from the GRIN lens, obtained using a knife-edge measurement. The blue points are experimental data and the red line is the obtained fit. **Right** tip-tilt mount hosting the GRIN lens.

## A.2. Mechanical components

Having a stable and reproducible optical alignment was of central importance for the project. The 3D Cavity showed in Fig. A.3 is derived from previously implemented designs. It additionally features a recess and clamps for the qubit chip for firmly fixing the qubit and guarantee an alignment w.r.t. laser as good as possible, holes of micrometers dimensions for shining the laser beam and pin holes that allow a quick and precise mount of the cavity onto the bracket. A similar design was also produced for the tunnel hosting the electrical resonator.

The custom bracket has a central role as all other components are hosted onto it (Fig. 3.6). The bracket features a slot for adjusting the position of the tilting mount, pins for fixing the cavity and screwing it onto the bracket and threaded holes for attaching the fiber collimator, collecting transmitted light.

## A.3. Fiber collimator

A fiber collimator is a device able to couple out the light from an optical fiber into a free-space beam, usually collimated, or to do the opposite. In our particular case the collimator was used to collect the light that was not absorbed or reflected by the superconducting device. If the input light is well aligned to the superconducting antenna, the device is not expected to collect much of the light, as scattering by the antenna causes low transmission and a chaotic transmitted beam profile. Should, however, thermal contractions lead to a significant misalignment of the laser beam from the antenna, the collimator will help mitigate heating effects by collecting the transmitted beam, as schematically shown, in Fig. A.4. The collimator used in this experiment (Schäfter + Kirchhoff 60FC-0-A3.1-00-Ti) was made of Titanium with a thermal expansion coefficient matching that of glass, to guarantee better performances at cryogenic temperatures. The

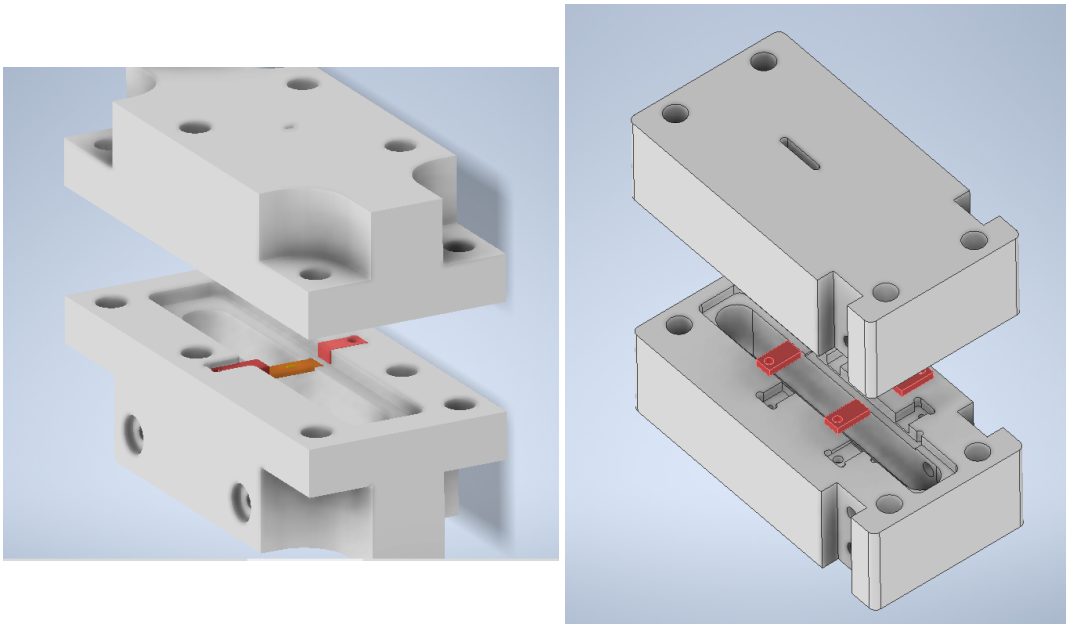

Figure A.3.: **Left** CAD view of the cavity hosting the qubit (yellow) and the qubit clamps (red) for fixing its position. **Right** CAD view of the resonator tunnel with the resonator clamps (red).

clear aperture of the device was 5 mm and it featured a $f = 3.1$ mm aspheric lens to reduce optical aberrations.

## A.4. Optical microscope

The optical infra-red (IR) microscope was developed during the course of a previous semester project and it allows us to image the laser position w.r.t. to the device under test at room temperature. As shown in Fig. A.5, the sample is illuminated in reflection through the microscope by a IR LED (Thorlabs - M810L4) working at a wavelength 810 nm to increase the imaging camera sensitivity. This LED light is first collimated by a $f = 20\,mm$ aspheric lens, it is then partially reflected by a 45:55 beam splitter (BS) and it is finally focused toward the sample by the $f = 20\,mm$ objective lens. After being reflected by the sample the light gets collimated back by the objective lens, is partially transmitted by the BS and is focused onto an IR camera (Gentec - Beamage 3.0) by the $f = 200\,mm$ tube lens. The microscope provides a $10\times$ magnification with a resolution $\sigma \approx 25\,\mu m$ . Fig. A.6 shows the microscope image of the qubit and the laser beam.

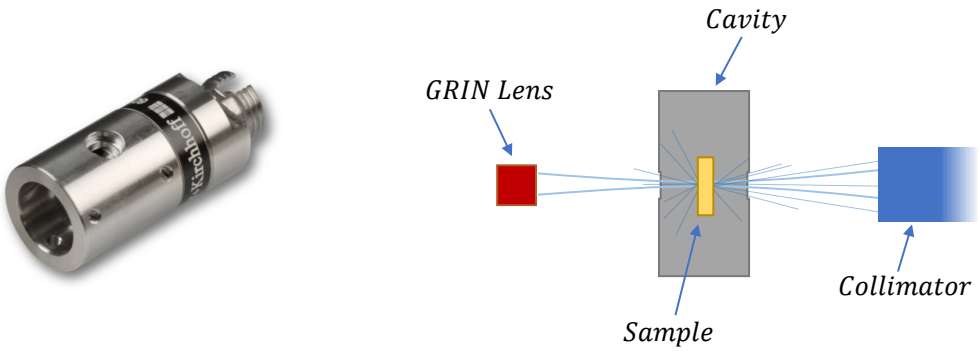


Figure A.4.: **Left** Fiber collimator image. **Right** Representation of the scattering and diffraction of the laser beam on the sample preventing an optimal light collection.

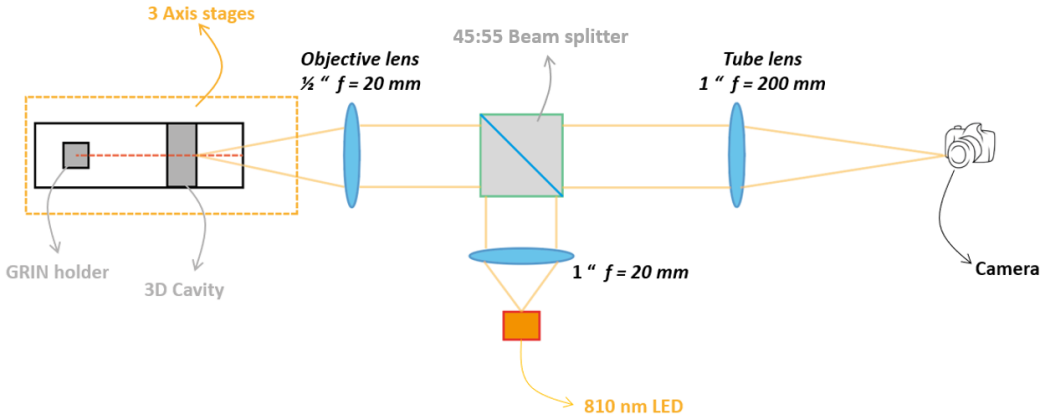


Figure A.5.: IR microscope schematic.

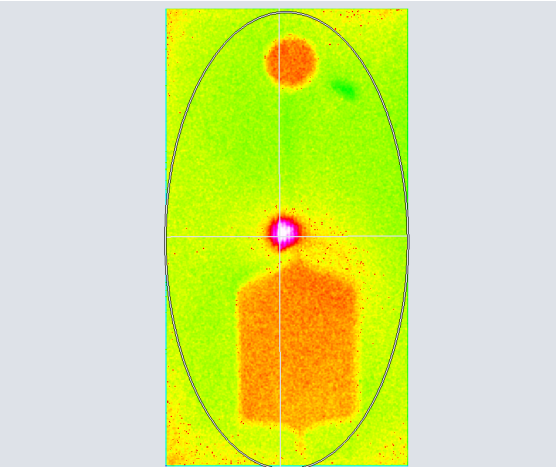

Figure A.6.: IR microscope image of the qubit. It is possible to see one of the qubit transmon pad with the circular antenna (orange) and the laser beam (red-white). Here the laser beam is intentionally misaligned to improve its visibility.

# Bibliography


1. Acın, A. *et al.* The quantum technologies roadmap: a European community view. *New Journal of Physics* **20,** 080201. https://doi.org/10.1088/1367-2630/aad1ea (Aug. 2018).
2. Arute, F. *et al.* Quantum supremacy using a programmable superconducting processor. *Nature* **574,** 505–510. https://doi.org/10.1038/s41586-019-1666-5 (2019).
3. Andersen, C. K. *et al.* Repeated quantum error detection in a surface code. *Nature Physics* **16,** 875–880. https://doi.org/10.1038/s41567-020-0920-y (2020).
4. Ma, W.-L. *et al. Quantum control of bosonic modes with superconducting circuits* 2021. arXiv: 2102.09668 [quant-ph].
5. Kimble, H. J. The quantum internet. *Nature* **453,** 1023–1030. http://dx.doi.org/10.1038/nature07127 (June 2008).
6. Guo, X. *et al.* Distributed quantum sensing in a continuous-variable entangled network. *Nature Physics* **16,** 281–284. http://dx.doi.org/10.1038/s41567-019-0743-x (Dec. 2019).
7. Magnard, P. *et al.* Microwave Quantum Link between Superconducting Circuits Housed in Spatially Separated Cryogenic Systems. *Phys. Rev. Lett.* **125,** 260502. https://link.aps.org/doi/10.1103/PhysRevLett.125.260502 (26 Dec. 2020).
8. Valivarthi, R. *et al.* Teleportation Systems Toward a Quantum Internet. *PRX Quantum* **1,** 020317. https://link.aps.org/doi/10.1103/PRXQuantum.1.020317 (2 Dec. 2020).
9. Miller, D. A. B. Attojoule Optoelectronics for Low-Energy Information Processing and Communications. *Journal of Lightwave Technology* **35,** 346–396 (2017).
10. Chu, Y. *et al.* Quantum acoustics with superconducting qubits. *Science* **358,** 199–202 (2017).
11. Kharel, P. *et al.* Multimode strong coupling in cavity optomechanics. arXiv: 1812.06202 [physics.optics] (2019).
12. Forsch, M. *et al.* Microwave-to-optics conversion using a mechanical oscillator in its quantum ground state. *Nature Physics* **16,** 69–74. https://doi.org/10.1038/s41567-019-0673-7 (Oct. 2019).
13. Mirhosseini, M., Sipahigil, A., Kalaee, M. & Painter, O. Superconducting qubit to optical photon transduction. *Nature* **588,** 599–603. https://doi.org/10.1038/s41586-020-3038-6 (Dec. 2020).

14. Kharel, P. *et al.* High-frequency cavity optomechanics using bulk acoustic phonons. *Science Advances* **5,** eaav0582. https://doi.org/10.1126/sciadv.aav0582 (2019).

15. Chu, Y. *et al.* Creation and control of multi-phonon Fock states in a bulk acoustic-wave resonator. *Nature* **563,** 666–670. https://doi.org/10.1038/s41586-018-0717-7 (2018).

16. Catelani, G., Schoelkopf, R. J., Devoret, M. H. & Glazman, L. I. Relaxation and frequency shifts induced by quasiparticles in superconducting qubits. *Phys. Rev. B* **84,** 064517. https://link.aps.org/doi/10.1103/PhysRevB.84.064517 (6 2011).

17. Glazman, L. & Catelani, G. Bogoliubov quasiparticles in superconducting qubits. *SciPost Physics Lecture Notes.* ISSN: 2590-1990. http://dx.doi.org/10.21468/SciPostPhysLectNotes.31 (June 2021).

18. Soldini, M. *Quasiparticles dynamics under infrared illumination* MA thesis (Hybrid Quantum Systems Group, ETH Zurich, 2020), 20.

19. Wang, C. *et al.* Measurement and control of quasiparticle dynamics in a superconducting qubit. *Nature Communications* **5.** https://doi.org/10.1038/ncomms6836 (2014).

20. Gao, J. *The Physics of Superconducting Microwave Resonators* en. PhD thesis (2008). https://resolver.caltech.edu/CaltechETD:etd-06092008-235549.

21. Chen. Laser Scanning Microscopy of Superconducting Lumped Element Resonators. **62,** 3–6. https://qudev.phys.ethz.ch/theses (2015).

22. Bardeen, J. Two-Fluid Model of Superconductivity. *Phys. Rev. Lett.* **1,** 399–400. https://link.aps.org/doi/10.1103/PhysRevLett.1.399 (11 Dec. 1958).

23. Werner, T. R., Falco, C. M. & Schuller, I. K. Impurity scattering time in aluminum. *Phys. Rev. B* **25,** 4510–4514. https://link.aps.org/doi/10.1103/PhysRevB.25.4510 (7 Apr. 1982).

24. Tinkham, M. *Introduction to Superconductivity* 2nd ed. ISBN: 0486435032. http://www.worldcat.org/isbn/0486435032 (Dover Publications, 2004).

25. Maxwell, E., Marcus, P. M. & Slater, J. C. Surface Impedance of Normal and Superconductors at 24,000 Megacycles per Second. *Phys. Rev.* **76,** 1332–1347. https://link.aps.org/doi/10.1103/PhysRev.76.1332 (9 1949).

26. Zhuravel, A. P. *et al.* Laser scanning microscopy of HTS films and devices (Review Article). *Low Temperature Physics* **32,** 592–607. https://doi.org/10.1063/1.2215376 (2006).

27. Axline, C. J. *Building Blocks for Modular Circuit QED Quantum Computing* PhD dissertation (Yale University, 2012).

28. Lutchyn, R., Glazman, L. & Larkin, A. Quasiparticle decay rate of Josephson charge qubit oscillations. *Phys. Rev. B* **72,** 014517. https://link.aps.org/doi/10.1103/PhysRevB.72.014517 (1 2005).

29. Serniak, K. *et al.* Hot Nonequilibrium Quasiparticles in Transmon Qubits. *Phys. Rev. Lett.* **121,** 157701. https://link.aps.org/doi/10.1103/PhysRevLett.121.157701 (15 2018).

30. Vepsäläinen, A. P. *et al.* Impact of ionizing radiation on superconducting qubit coherence. *Nature* **584,** 551–556. https://doi.org/10.1038/s41586-020-2619-8 (2020).

31. Yang, Y. *Characterizing electromechanical coupling with multiplexed spectroscopy* MA thesis (Hybrid Quantum Systems Group, ETH Zurich, 2020).

32. Bernasconi, A. C. *Designing Acoustic Mode Shapes for Microwave to Optical Transduction* MA thesis (Hybrid Quantum Systems Group, ETH Zurich, 2021), 62.

33. Koch, J. *et al.* Charge-insensitive qubit design derived from the Cooper pair box. *Phys. Rev. A* **76,** 042319. https://link.aps.org/doi/10.1103/PhysRevA.76.042319 (4 Oct. 2007).

34. M. H. Devoret A. Wallraff, J. M. M. Superconducting Qubits: A Short Review. https://arxiv.org/abs/cond-mat/0411174 (Nov. 2004).

35. Schuster, D. I. *et al.* Resolving photon number states in a superconducting circuit. *Nature* **445,** 515–518. https://doi.org/10.1038/nature05461 (Feb. 2007).

36. Paik, H. *et al.* Observation of High Coherence in Josephson Junction Qubits Measured in a Three-Dimensional Circuit QED Architecture. *Phys. Rev. Lett.* **107,** 240501. https://link.aps.org/doi/10.1103/PhysRevLett.107.240501 (24 Dec. 2011).

37. Haroche, S. & Raimond, J.-M. *Exploring the Quantum* https://doi.org/10.1093/acprof:oso/9780198509141.001.0001 (Oxford University Press, Aug. 2006).

38. Blais, A., Huang, R.-S., Wallraff, A., Girvin, S. M. & Schoelkopf, R. J. Cavity quantum electrodynamics for superconducting electrical circuits: An architecture for quantum computation. *Phys. Rev. A* **69,** 062320. https://link.aps.org/doi/10.1103/PhysRevA.69.062320 (6 June 2004).

39. Wallraff, A. *et al.* Strong coupling of a single photon to a superconducting qubit using circuit quantum electrodynamics. *Nature* **431,** 162–167. https://doi.org/10.1038/nature02851 (Sept. 2004).

40. Girvin, S. M. in *Quantum Machines: Measurement and Control of Engineered Quantum Systems* 113–256 (Oxford University Press, June 2014). https://doi.org/10.1093/acprof:oso/9780199681181.003.0003.

41. Majer, J. *et al.* Coupling superconducting qubits via a cavity bus. *Nature* **449,** 443–447. https://doi.org/10.1038/nature06184 (Sept. 2007).

42. Minev, Z. K. *et al. Energy-participation quantization of Josephson circuits* 2021. arXiv: 2010.00620 [quant-ph].

43. Vollenweider, S. *A cryogenic optical cavity for Brillouin cavity optomechanics* MA thesis (Hybrid Quantum Systems Group, ETH Zurich, 2020), 74.